TRIMS LST: A daily 1-km all-weather land surface temperature dataset for the Chinese landmass and surrounding areas (2000-2021)

Wenbin Tang[1], Ji Zhou[1], Jin Ma[1], Ziwei Wang[1], Lirong Ding[1], Xiaodong Zhang[2, 3], Xu Zhang[1]

[1] School of Resources and Environment, University of Electronic Science and Technology of China, Chengdu 611731, China
[2] Shanghai Aerospace Electronic Technology Institute, Shanghai 201109, China
[3] Shanghai Spaceflight Institute of TT&C and Telecommunication, Shanghai 201109, China

Correspondence to: Ji Zhou (jzhou233@uestc.edu.cn)

Abstract. Land surface temperature (LST) is a key variable within the Earth's climate system and a necessary input parameter required by numerous land-atmosphere models. It can be directly retrieved from satellite thermal infrared (TIR) observations, but cloud contamination results in many spatial missing. To investigate the temporal and spatial variations of LST in China, long-term, high-quality, and spatio-temporally continuous LST datasets (i.e., all-weather LST) are urgently needed. Fusing satellite TIR LST and reanalysis datasets is a viable route to obtain long time-series all-weather LST. Among satellite TIR LSTs, the MODIS LST is the most commonly used and a few all-weather LST products generated in this way have been reported recently. However, the publicly reported all-weather LSTs are not available during the temporal gaps of MODIS between 2000 and 2002. In this context, we report a daily 1-km all-weather LST dataset for the Chinese landmass and surrounding areas – TRIMS LST. Different from other products, the TRIMS LST begins on the first day of the new millennium (i.e., January 1, 2000). The TRIMS LST was generated based on the Enhanced Reanalysis and Thermal infrared remote sensing Merging (E-RTM) method. Specifically, the original RTM method was used to generate the TRIMS LST outside the temporal gaps. Two newly developed approaches, including the Random-Forest based Spatio-Temporal Merging (RFSTM) approach and Time-Sequential LST based Reconstruction (TSETR) approach, were used to produce Terra/MODIS-based and Aqua/MODIS-based TRIMS LSTs during the temporal gaps, respectively. Thorough evaluation of the TRIMS LST was conducted. A comparison with the GLDAS and ERA5-Land LSTs demonstrates that TRIMS LST has similar spatial patterns but higher image quality, more spatial details, and no evident spatial discontinuities. Further comparison with MODIS and AATSR LSTs shows that TRIMS LSTs agree well with them, with mean bias deviation (MBD) between -0.40 K and 0.30 K and standard deviation of bias (STD) between 1.17 K and 1.50 K. Validation based on ground measured LST at 19 ground sites showed that the mean bias error (MBE) of the TRIMS LST ranged from -2.26 K to 1.73 K and the root mean square error (RMSE) was 0.80 K to 3.68 K, with no significant difference between the clear-sky and cloudy conditions. The TRIMS LST has already been used by scientific communities in various applications such as soil moisture downscaling, evapotranspiration estimation, and urban heat island (UHI) modelling. The TRIMS LST is freely and conveniently available at https://doi.org/10.11888/Meteoro.tpdc.271252 (Zhou et al., 2021).

1 Introduction

Land surface temperature (LST) is a key variable related to the energy exchange at the interface between the land surface and
35 the atmosphere. It is the result of the thermal feedback of various ground surface to incident solar radiation and atmospheric
downward radiation. Therefore, it is a necessary input parameter required by numerous land–atmosphere models (Jiang and
Liu, 2014; Li et al., 2013b, 2023b). LST have been widely used in a variety of studies, such as surface evapotranspiration (ET)
estimation (Anderson et al., 2011; Ma et al., 2022), urban heat island (UHI) modelling (Alexander, 2020; Liao et al., 2022),
drought monitoring (Zhang et al., 2017), and ecological assessment (Sims et al., 2008).

40 In the past four decades, especially since the beginning of the new millennium (i.e., 2000), China and its surrounding areas
have experienced rapid economic development and population growth, accompanied by notable changes to the natural
environment (Yang and Huang, 2021). Meanwhile, China has adopted a series of interventions to protect the environment
since the 1980s, such as the Grain to Green Program (Wang et al., 2017), Three-North Shelter Forest Program (Zhai et al.,
2023), and Red Lines of Cropland (a policy to ensure that Chinese arable land does not drop below 120 million hectares).

45 These interventions have played a key role in changing the land use/cover and the regulating climate change (Chen et al.,
2019a). In addition, with the warming climate, extreme weather and meteorological disasters occur frequently in China and its
surrounding areas (Chen et al., 2019b). Since LST is highly sensitive to land cover change, heat waves, droughts, and
vegetation information and is an indicator of global climate change (Mildrexler et al., 2018; Peng et al., 2014), it is important
to investigate the spatial and temporal variations of LST for these areas. This requires a long-term, high-quality, and spatio-
50 temporally continuous LST dataset.

LST can be obtained through *in-situ* observations, model simulations, and remote sensing retrievals. However, LST is highly
spatially and temporally heterogeneous and affected by various factors such as land cover, soil type, topography, climatic, and
meteorological conditions (Liu et al., 2006; Zhan et al., 2013). *In-situ* observations based on spatial 'point measurement' are
not able to obtain spatially continuous LSTs, and the current model simulation suffer from coarse spatial resolution. In contrast,
55 satellite remote sensing, which has advantages of better spatial continuity, larger coverage, good ability for repeating
observations, and much higher spatial resolution, has become an important way to obtain LST for large areas (Li et al., 2013b).
Satellite thermal infrared (TIR) remote sensing can directly obtain the regional and global LST efficiently. A series of satellite
TIR LST products are currently available to users, including platforms such as polar orbiting and geostationary satellite
platforms. Among the satellite TIR LST products, the MODIS LST products is the most widely used because of its global
60 coverage, long time-series (since February 24, 2000 for Terra and since July 4, 2002 for Aqua), high quality, and good
accuracy (Aguilar-Lome et al., 2019; Sandeep et al., 2021; Wan, 2014).

Although MODIS LST products (especially with a 1-km spatial resolution) have shown good performance in related
applications, they generally have significant spatial absences due to cloud contamination, especially in low and middle latitudes
in China (e.g., the Tibet Plateau and southern China) (Duan et al., 2017). Cloud contamination restricts the LST products from

65   playing a more critical role in subsequent applications (Li et al., 2023b). Furthermore, Terra/Aqua MODIS has temporal gaps in 2000-2002; thus, it is not easy to generate the all-weather LST products during these gaps.

In recent years, many methods have been developed to generate all-weather LSTs based on satellite TIR LSTs and other data (Jia et al., 2022; Zhang et al., 2022). Typical methods include spatial-temporal interpolation, surface energy balance (SEB), and multisource data integration. The spatial-temporal interpolation methods take advantage of temporal variation patterns of

70   the LST as well as the spatial characteristics. However, the results obtained by the above methods are the hypothetical LSTs under clear-sky conditions, not the LST under the cloud-contaminated regions. LST (Martins et al., 2019). To solve the above problems, SEB is proposed as physical method (Jin and Dickinson, 2000). Under cloudy conditions, this method considers longwave radiation and solar radiation as influences on the LST. Martins et al. (2019) used the SEB method to successfully fill the missing LSTs using land surface parameters provided by the European Satellite Application Facility on Land Surface

75   Analysis (LSA-SAF) and generate the all-weather LST product (MLST-AS). In addition, a more general approach that incorporates the clear-sky LSTs into the SEB has recently been developed to estimate the LSTs under cloud- contaminated regions based on the MODIS and Visible infrared Imaging Radiometer (VIIRS) data (Jia et al., 2021).

At present, multisource data integration methods have been widely used to generate seamless all-weather LSTs. Present multisource data fusion methods mainly to integrate TIR LSTs with satellite passive microwave (PMW) observation or

80   reanalysis data. PMW data can be used for estimating all-weather LST retrievals because they are able to observe LST information under cloud-contaminated regions (Holmes et al., 2009; Zhou et al., 2017). However, there are limitations in obtaining all-weather LST from PMW observations. First, the spatial resolution of PMW data differs significantly from TIR, such as the Advanced Microwave Scanning Radiometer 2 (AMSR2) with ~10 km spatial resolution. the spatial coverage of the PMW data is incomplete because there are orbital gaps. Third, the temperature information retrieved from PMW

85   observations contains information from the subsurface, which is physically different from the TIR LST, which provides the skin temperature (Zhou et al., 2017). Compared with the PMW data, reanalysis data can provide spatially continuous LSTs and related surface parameters; thus, it can act as an alternative basis to obtain the all-weather LST (Long et al., 2020; Ding et al., 2022). A typical method is the Reanalysis and Thermal infrared remote sensing Merging (RTM) method proposed by Zhang et al. (2021) for integrating the GLDAS and MODIS LSTs for the Tibetan Plateau.

90   In recent years, based on the aforementioned three typical methods, various all-weather LST datasets were released (Duan et al., 2017; Hong et al., 2022; Jia et al., 2022; Li et al., 2021a; Metz et al., 2017; Muñoz-Sabater et al., 2021; Yao et al., 2023; Yu et al., 2022). However, all-weather LST data with both high temporal resolution (4 observations per day or higher) and high resolution (1 km or higher) since 2000 for the Chinese landmass and the surrounding areas are still rare.

In this study, we proposed the enhanced RTM (E-RTM) method to produce a daily (four observations per day) 1-km all-

95   weather LST dataset for the Chinese landmass and surrounding areas (19°N-55°N, 72°E-135°E), which is known as the Thermal and Reanalysis Integrating Moderate-resolution Spatial- seamless LST (TRIMS LST). The E-RTM method includes three modules (Sect.3). The original RTM method is used to produce the TRIMS LST outside the temporal gaps. Additionally, based on the physical properties of the LST time component decomposition model, Terra/MODIS-based and Aqua/MODIS-

based TRIMS LST during the temporal gaps are produced. TRIMS LST was evaluated in this study using *in-situ* sites to

100   provide better-quality data for the study of Urban thermal environment, meteorology and hydrology.

2 Datasets

2.1 Satellite data and reanalysis data

In this study, the main satellite data used are the 1-km daily MODIS LST/emissivity product (MOD11A1: February 2000 to December 2021; MYD11A1: July 2002 to December 2021) in version 6.1. This LST product was produced based on the

105   generalized split-window algorithm and has good accuracy for homogeneous surfaces (Wan, 2014). As mentioned previously, it is usually used as the basis in the reconstruction of all-weather LSTs. In this study, this product is also used as a basis data for producing the TRIMS LST. The other used MODIS datasets used include: (1) the 1-km 16-day Normalized Difference Vegetation Index (NDVI) product (MOD13A2: February 2000 to December 2021) in version 6.1; (2) the 500-m daily Normalized Difference Snow Index (NDSI) product(MOD10A1: February 2000 to December 2021) in version 6; and (3) the

110   500-m daily MODIS land surface albedo product (MCD43A3: February 2000 to December 2021) in version 6.1. All of the above products are available at EARTHDATA (https://earthdata.nasa.gov/). In addition to generation and evaluation of the all-weather LST, we also collected (1) the 90-m Shuttle Radar Topography Mission Digital Elevation Model data (SRTM DEM; http://srtm.csi.cgiar.org); (2) the 30-m yearly China land cover dataset (2000-2015) from Zenodo (CLCD, https://doi.org/10.5281/zenodo.4417810) (Yang and Huang, 2021) and (3) the 1-km daily ENVISAT/AATSR LST product

115   (May 2002 - April 2012) (https://www.ceda.ac.uk/).

The main reanalysis data used in this study are the Global Land Data Assimilation System assimilation (GLDAS) data provided by the Goddard Earth Sciences Data and Information Services Center (GES DISC) (Rodell et al., 2004). Specifically, the 0.25° 3-hourly LST from the GLDAS Noah model between January 2000 and December 2021 was used as another input of the RTM method. In addition, we also collected the 0.1° hourly ERA5-Land LST data (Muñoz-Sabater et al., 2021), and its LST was be

120   compared with the generated TRIMS LST.

2.2 Ground measurements

Table I shows 19 ground sites that recorded longwave radiation data for different time spans. According to geographical locations and land cover types provided in Table I, it is clear that they are distributed in different climate zones. This indicates that they encompass a wide range of land surface and climatic situations for adequate validation of the TRIMS LST. The

125   measurement device at the selected ground station includes a long-wave radiometer and four-component radiometers, including CNR1, CNR4, and CG4 (Kipp & Zonen, Netherlands; https://www.kippzonen.com/). According to the specifications of these radiometers, the uncertainties in daily total for longwave radiation measurements are 3% - 10%. With the measured incoming and outgoing longwave radiation, the LST of the land cover type within the field-of-view (FOV) of the radiometer can be calculated through the radiative transfer equation in the form of the Stephan-Boltzmann's law (Ma et al., 2021).

130 Considering the uncertainties of the longwave radiation measurement, the uncertainties of the calculated *in-situ* LSTs are approximately 0.6 K-1.2 K (Xu et al., 2013; Yang et al., 2020; Ma et al., 2021).

Spatial representativeness of ground sites has different degrees of influence on validation of TIR-based LST using *in-situ* LST. In this study, a newly developed indicator (μ_{REP}) proposed by Ma et al. (2021) was implemented to carefully quantify the spatial representativeness of each site. For the 19 sites, the calculated μ_{REP} was 0.31 K to 0.83 K, indicating good to acceptable

135 representativeness of these sites for the validation of a 1-km LST.

Table I: Details of the 19 selected ground sites and their measurements.

Site	Latitude and Longitude (°N, °E)	Elevation (m)	Radiometers	Height (m)	Diameter (m)	Surface type	Period	μ_{REP} (K)	Source
Arou (ARO)	38.05, 100.46	3033	CNR4	5	37.32	Subalpine meadow	2013-2021	0.82	HiWATER
Daman (DAM)	38.86, 100.37	1556	CNR1	12	89.57	Farmland	2013-2021	0.31	HiWATER
Desert (DET)	42.11, 100.99	1054	CNR4	6	44.78	Desert	2015-2021	0.45	HiWATER
Dashalong (DSL)	38.84, 98.94	3739	CNR4	6	44.78	Marsh alpine meadow	2013-2021	0.54	HiWATER
Ebao (EBA)	37.95, 100.92	3294	CNR1	6	44.78	Alpine Meadow	2013-2016	0.61	HiWATER
Gobi (GOB)	38.92, 100.31	1562	CNR1	6	44.78	Gobi	2013-2015	0.33	HiWATER
Huazhaizi (HZZ)	38.77, 100.32	1735	CNR1	6	44.78	Desert	2015-2021	0.35	HiWATER
Sidaoqiao (SDQ)	42.00, 101.14	873	CNR1	10	74.64	Tamarix	2013-2021	0.82	HiWATER
Shenshawo (SSW)	38.79, 100.49	1555	CNR1	6	44.78	Desert	2014-2015	0.42	HiWATER
Huailai (HLA)	40.35, 115.79	480	CNR4	5	37.32	Farmland	2013-2020	0.81	HBE
D105	33.06, 91.95	5039	CNR1	1.34	10.00	Subalpine meadow	2002-2004	0.82	CEOP-CAMP
Gaize (GAZ)	32.31, 84.06	4416	CNR1	1.49	11.12	Barren land	2002-2004	0.80	CEOP-CAMP
Guantao(GUT)	36.52, 115.13	30	CNR1	15.7	117.19	Farmland	2009-2010	0.72	HBE
Changbaishan (CBS)	42.40, 128.10	736	CNR1	6*	44.78	Mixed forest	2003-2005	0.83	China Flux
Daxing (DXI)	39.62, 116.43	20	CNR1	28	208.99	Farmland	2008-2010	0.78	HBE
Dinghushan (DHS)	23.17, 112.53	300	CNR1	19*	141.82	Broad-leaved evergreen forest	2003-2005	0.44	CERN
Maqu (MQU)	33.89, 102.14	3423	CNR1	1.5	11.20	Grassland	2010	0.56	NIEER-CAS
Qianyanzhou (QYZ)	26.74, 115.06	75	CNR1	1.8	13.44	Evergreen coniferous forest	2003-2005	0.52	CERN
Tongyu (TYU)	44.42, 122.87	184	CG4	3	22.39	Farmland	2003-2004	0.49	CEOP-CAMP

Note: The ground sites were operated by different field campaigns or programs. CERN: Chinese Ecosystem Research Network (Pastorello et al., 2020); CEOP-CAMP: the Coordinated Energy and
140 Water Cycle Observation Project (CEOP) and Asia-Australia Monsoon Project (CAMP) (Ma et al., 2006; Liu et al., 2004); China Flux (Pastorello et al., 2020; Zhang and Han, 2016); HBE: Haihe experiment (Guo et al., 2020; Liu et al., 2013); HiWATER: Heihe Watershed Allied Telemetry Experimental Research (Che et al., 2019; Li et al., 2013a; Liu et al., 2011, 2018); NIEER-CAS: Northwest Institute of Eco-Environment and Resources, Chinese Academy of Sciences (Wen et al., 2011).

Earth System
Science
Data

Open Access

Discussions

3. Methodology

145 TRIMS LST is generated based on the E-RTM method, which contains three modules as shown in Fig.1. Module I runs the original RTM method (Zhang et al., 2021) to produce the daily all-weather LST at the Terra (Aqua) satellite overpass time from DOY 55 of 2000 (DOY 185 of 2002) to DOY365 of 2021 by merging MOD11A1 (MYD11A1) and GLDAS LSTs. Module II extends the beginning date of the MOD11A1 LST based all-weather LST to January 1 2000 through a Random-Forest based Spatio-Temporal Merging (RFSTM) approach. Module III extends the beginning date of the MYD11A1 LST 150 based all-weather LST to January 1 through a Time-Sequential LST based Reconstruction (TSETR) approach.

3.1 Module I: the RTM method

Details of the RTM method can be found in Zhang et al. (2021). For the convenience of readers, a brief description of RTM is provided here. In the temporal dimension, the time series of LST can be expressed as:

$$LST(t_{d}, t_{avg}, t_{ins}) = LFC(t_{d}, t_{avg}) + HFC(t_{d}, t_{avg}, t_{ins}) + HFC_{cld}(t_{d}, t_{ins}), \quad (1)$$

155 where t_d is the day of year (DOY); t_{ins} is overpass time of a TIR sensor (i.e., MODIS) and t_{avg} is the average observation time calculated from t_{ins}; LFC is the low frequency component that represents the intra-annual variation component of the LST under ideal clear-sky conditions; HFC is the high frequency component, which represents the sum of the diurnal LST variation and the weather variation component (WTC) under ideal clear-sky conditions; HFC_{cld} is a correction term representing the impact on LST triggered by cloud contamination under cloudy conditions; and HFC_{cld} is equal to zero under clear-sky 160 conditions. In the RTM method, LFC, HFC, and HFC_{cld} in Eq.(1) are first determined from the MODIS LST and the GLDAS LST. Then, the optimized models are determined for the three components according to their characteristics and their quality is improved by inputting their descriptors. Finally, three optimized components are integrated to generate the all-weather LST.

3.2 Module II: the RFSTM approach

The RFSTM approach was developed to predict the all-weather LST during the period of DOY 1-54 2000 during which the 165 Terra/MODIS LSTs were not available. It is based on the fact that (i) the LST of a pixel in the temporal dimension is strongly affected by the meteorological conditions as well as the its underlying surface and (ii) the LSTs of many pixels at a certain time are closely related to their underlying surfaces (Ma et al., 2021). Therefore, RFSTM has two stages, namely, the temporal stage and the spatial stage.
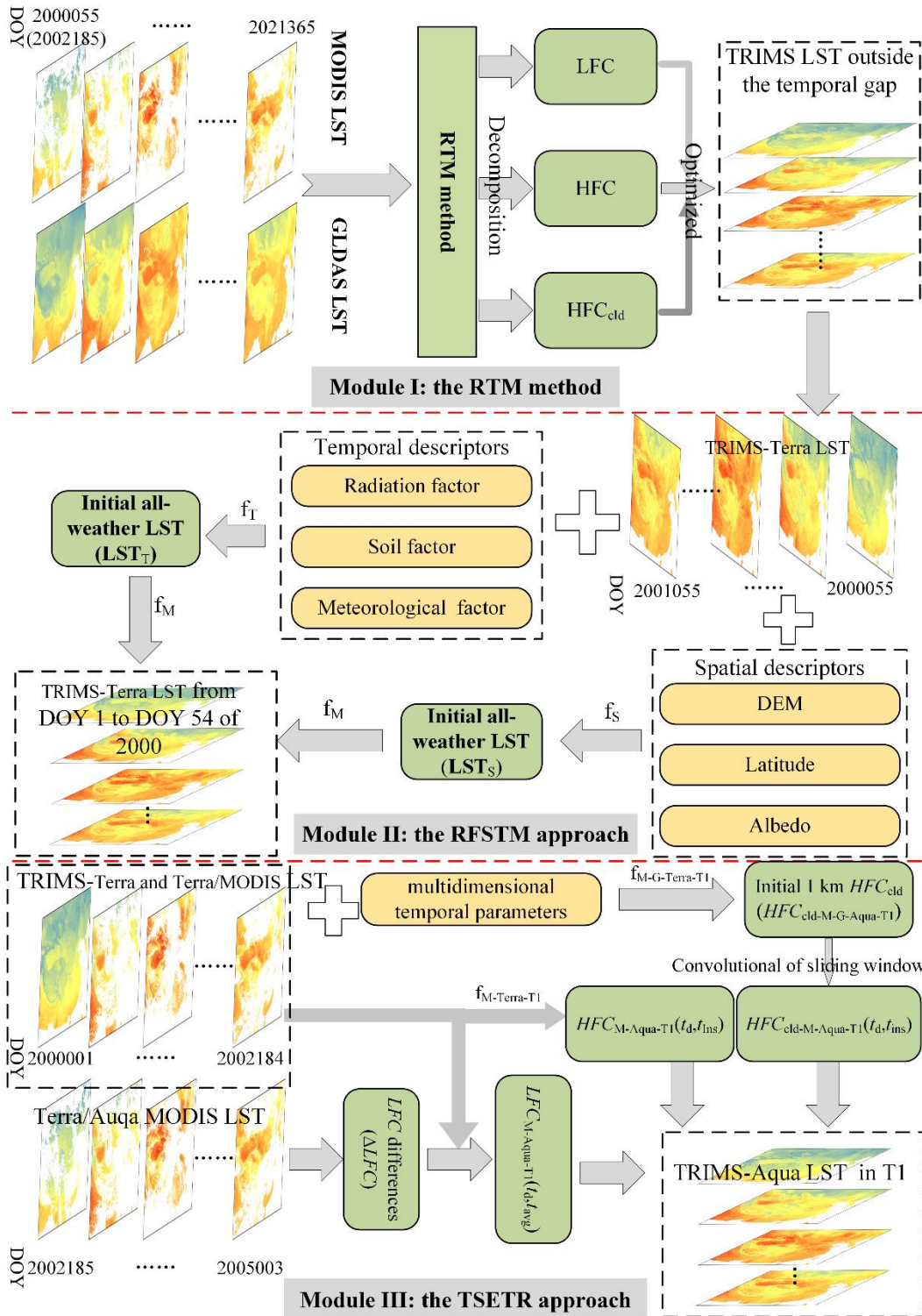
170

Figure 1: Flowchart of the E-RTM method. Note that the date in this figure is in the format of YYYY+DOY.

In the temporal stage, the daily LSTs ($\mathbf{LST_T}$) of a pixel Q in a certain period are modelled as:

$$\mathbf{LST_T} = f_T(\mathbf{X_T})$$

$$\mathbf{X_T} = [\mathbf{P_{T\text{-}1}} \; \mathbf{P_{T\text{-}2}} \; ... \; \mathbf{P_{T\text{-}m}}]^T$$

$$= \begin{bmatrix} p_{T\text{-}1}(t_{d\text{-}1}) & p_{T\text{-}1}(t_{d\text{-}2}) & \cdots & p_{T\text{-}1}(t_{d\text{-}n}) \\ p_{T\text{-}2}(t_{d\text{-}1}) & p_{T\text{-}2}(t_{d\text{-}2}) & \cdots & p_{T\text{-}2}(t_{d\text{-}n}) \\ \cdots & \cdots & & \cdots \\ p_{T\text{-}m}(t_{d\text{-}1}) & p_{T\text{-}m}(t_{d\text{-}2}) & \cdots & p_{T\text{-}m}(t_{d\text{-}n}) \end{bmatrix} \tag{2}$$

where the subscript T denotes the temporal stage; the function f_T expresses the mapping in temporal dimensions from
175   descriptors to LST; $\mathbf{X_T}$ denotes the matrix including LST descriptors' time series ($\mathbf{P_{T\text{-}i}}$, $i=1, 2, ..., m$); and n is the number of
days within the temporal gap of Terra MODIS LST.

Since the MODIS LST is not available as a reference for reconstruction and it is impossible to identify the different weather
conditions (e.g., clear-sky and cloudy conditions), we used the mapping function f_T to predict the 1-km all-weather LST.
However, the relationship between LST and its descriptors cannot currently be analytically expressed currently. Fortunately,
180   the machine learning has been reported to be effective in enhancing the spatial resolution of remote sensing images.
Specifically, the random forest (RF) algorithm has shown good performance in mapping the correlation between LST with
finer resolution and its descriptors with coarser resolution (Li et al., 2021a; Xu et al., 2021; Zhao and Duan, 2020). Therefore,
the RF algorithm was employed here to realize f_T. The temporal descriptors of LST include net longwave radiation, downward
longwave flux, soil moisture profile (e.g., surface, 0-10 cm and 10-40 cm in GLDAS NOAH model-based data), wind-speed,
185   soil temperature profile (e.g., surface, 0-10cm and 10-40 cm in GLDAS NOAH-model based data), air temperature and albedo.
The training period for f_T with RF was set as DOY 55 of 2000 to DOY 55 of 2001 (366 days in total), and the prediction period
for $\mathbf{LST_T}$ was from DOY 1 of 2000 to DOY 54 of 2000.

Considering that LST varies in both temporal and spatial dimensions, the spatial descriptors of LST should also be considered.
Therefore, in the spatial stage, the LSTs ($\mathbf{LST_S}$) at t_d in the prediction period are expressed as:

190    $$\mathbf{LST_S} = f_S[N_{S\text{-}1}(t_d) \; N_{S\text{-}2}(t_d) \; ... \; N_{S\text{-}k}(t_d)], \tag{3}$$

where the subscript S denotes the spatial stage; the function f_S expresses the mapping in spatial dimensions from the descriptors
to LST; k is the number of spatial descriptors of LST; and N_S denotes the 1-km spatial descriptor of LST ($N_{S\text{-}i}$, $i=1, 2, ..., k$).
The spatial descriptors of LST include the DEM, latitude, and albedo. Note that (i) all the descriptors selected in the spatial
stage are from the ancillary data with a high resolution (i.e., 1 km in this study); (ii) the albedo was selected in this algorithm
195   because it involves the related information of surface emissivity such as vegetation growth, surface and subsurface moisture
profiles and ground cover types. In the spatial stage, for a specific day (t_d), classify the target is classified into several subareas,
including thick vegetation, sparse vegetation, barren land areas, snow-ice areas and water, using the1-km NDVI and NDSI.
Then, for each subarea, the spatial descriptors of LST are input into f_S via Eq. (3). Note that f_S with RF is trained with the 1-
km LST and spatial descriptors of a day, and has (i) has the same observation time as t_d and (ii) has the smallest difference in
200   the number of days between t_d.

To involve all spatio-temporal LST descriptors and guarantee the best performance of the output, the LSTs ($\mathbf{LST}_T$ and $\mathbf{LST}_S$) need to be merged together to derive the final 1-km LST($\mathbf{LST}_M$):

$$\mathbf{LST}_M = f_M(\mathbf{LST}_T, \mathbf{LST}_S), \tag{4}$$

where f_M denotes the RF-based mapping which indicates the contributions to the $\mathbf{LST}_M$ from $\mathbf{LST}_T$ and $\mathbf{LST}_S$, respectively.

205 For a single 1-km pixel, the RF-based regression contribution function is trained using $\mathbf{LST}_T$ (obtained by Eq. 2), $\mathbf{LST}_S$ (obtained by Eq. 3) and TRIMS LST in the training period. Then, f_C is applied to estimate the 1-km all-weather LST in the prediction period via Eq. (4).

3.3 Module III: the TSETR approach

The TSETR approach was developed to estimate the all-weather LST during the period from DOY 1 of 2000 to DOY 184 of
210 2002 during which the Aqua/MODIS LSTs were not available (with a temporal gap of 915 days). Previous studies have shown that it is possible to convert between the Terra MODIS LSTs and Aqua MODIS LST, considering land cover types, geolocation and season (Coops et al., 2007). Therefore, Terra/MODIS LSTs from 2000-2002 could be transformed to Aqua/MODIS LSTs (Li et al., 2018). Since the Terra/MODIS LST (MOD11A1) is available as a reference in the temporal gap, we generated an all-weather LST based on the TSETR approach, which is reconstruction rather than prediction.

215 According to Eq. (1), the LST time series can be decomposed into *LFC*, *HFC* and HFC_{cld} under all-weather conditions. Therefore, the TSETR approach has three stages. In the first stage, we need to estimate the *LFC* during the temporal gap at the Aqua overpass time. In this case, the temporal gap period was set as T1, and DOY 185 of 2002 to DOY 3 of 2005 was set as T2 (Fig.2). According to the analytical expression and physical meaning of *LFC*, there is no underlying trends of change within the three annual parameters (T_{avg}, *A* and ω) except for the periodic variation in the LST, which means that the *LFC* is cyclic-
220 stationary over a short time period (Bechtel, 2015; Weng and Fu, 2014; Zhu et al., 2022). Once the three annual parameters are determined, the *LFC* can be calculated for a given day.

Therefore, in the TSETR approach, we assume that the *LFC* differences (ΔLFC) between the Terra and Aqua overpass times in T1 and T2 are also cyclic-stationary. In T2, the *LFC* at the Terra/MODIS and Aqua/MODIS pixels are determined separately. In T1, the *LFC* at the Aqua overpass time of the pixel M can be expressed as:

225
$$\begin{cases} LFC_{M\text{-}Aqua\text{-}T1}(t_d, t_{avg}) = LFC_{M\text{-}Terra\text{-}T1}(t_d, t_{avg}) + \Delta LFC_M(t'_d, t_{avg}) \\ \Delta LFC_M(t'_d, t_{avg}) = LFC_{M\text{-}Aqua\text{-}T2}(t'_d, t_{avg}) - LFC_{M\text{-}Terra\text{-}T2}(t'_d, t_{avg}) \end{cases}, \tag{5}$$

where t_d is a specific day in T1; t'_d is a specific day corresponding to t_d in T2; $LFC_{M\text{-}Aqua\text{-}T1}(t_d,t_{avg})$ and $LFC_{M\text{-}Terra\text{-}T1}(t_d,t_{avg})$ denote the *LFC* corresponding to the Aqua/Terra overpass time in T1, respectively; and $LFC_{M\text{-}Aqua\text{-}T2}(t'_d,t_{avg})$ and $LFC_{M\text{-}Terra\text{-}T2}(t'_d,t_{avg})$ denote the *LFC* corresponding to the Aqua and Terra overpass time in T2, respectively.
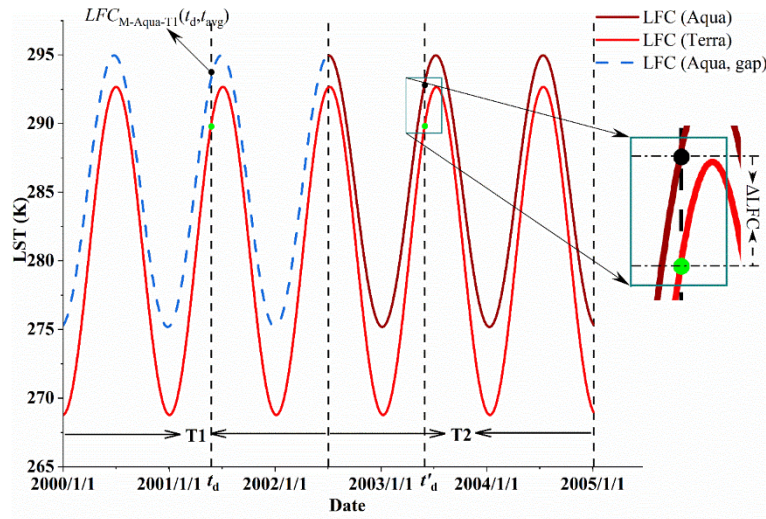
230 **Figure 2: Schematic diagram for estimating *LFC* in T1.**

HFC is estimated in the original RTM method using a nonlinear mapping established by multiple descriptors. In the second stage of E-RTM, the *HFC* within TI at the Aqua overpass time can be estimated by using its descriptors through RF (Xu et al., 2021).

$$HFC_{\text{M-Aqua-T1}}(t_d, t_{ins}) = f_{\text{M-Terra-T1}}(lat_M, lon_M, DEM_M, NDVI_M(t_d), slp_M(t_d), \alpha_M(t_d), \Delta t_M(t_d), v_M(t_d)), \tag{6}$$

235 where lat_M, lon_M, DEM_M, $NDVI_M$, slp_M, α_M, Δt_M and v_M are the latitude, longitude, DEM, NDVI, slope, albedo, difference between t_{ins} and t_{avg} , and the atmospheric water vapour content, respectively; and $f_{\text{M-Terra-T1}}$ is an RF mapping model based on Terra MODIS data and its corresponding descriptors in T1.

In Eq.(6), $f_{\text{M-Terra-T1}}$ can be applied to estimate the *HFC* at the Aqua overpass time for the following reasons. First, the LSTs of the same pixel at different moments of a given day also meet the criteria condition of similar pixels in the RTM method

240 (Zhang et al., 2021). This is the theoretical basis for the possibility of conversion between Terra/MODIS LSTs and Aqua/MODIS LSTs (Li et al., 2018), and according to the meaning of the *HFC* and the parameterization scheme, it should be highly correlated between similar pixels. Second, the factors used to build the mapping model can portray the effects of diurnal LST variation (Δt_M) and weather variation (v_M).

In the third stage, we need to estimate the HFC_{cld} within the temporal gap period at the Aqua overpass time. In fact, HFC_{cld} is

245 essentially an atmospheric correction term and it is obtained from the GLDAS LST in the RTM method. According to the parameterization scheme of the RTM method, the clear-sky MODIS pixels and their corresponding GLDAS LSTs are the necessary inputs for the estimation of HFC_{cld}. It is not possible to obtain HFC_{cld} directly in this stage due to the lack of Aqua/MODIS in T1.

Inspired by the Temporal Component Decomposition (TCD) method (Zhang et al., 2019) and other methods integrating PMW

250 and TIR LST (Parinussa et al., 2016; Zhang et al., 2020), the initial value of the 1-km HFC_{cld} can be expressed as:

$$HFC_{\text{cld-M-G-Auqa-T1}}(t_d, t_{ins}) = LST_{\text{M-G-Auqa-T1}}(t_d, t_{ins}) - LFC_{\text{M-Auqa-T1}}(t_d, t_{avg}) - HFC_{\text{M-Auqa-T1}}(t_d, t_{ins}), \tag{7}$$

where $HFC_{\text{cld-M-G-Aqua-T1}}$ is the initial 1-km HFC_{cld} of M; and $LST_{\text{M-G-Aqua-T1}}$ is the initial 1-km LST of M under all-weather conditions. In this stage, the LST-related multidimensional temporal parameters are selected from GLDAS and an expression such as Eq. (2) is established for estimating $LST_{\text{M-G-Aqua-T1}}$:

$$LST_{\text{M-G-Auqa-T1}}(t_d, t_{ins}) = f_{\text{M-G-Terra-T1}}(Lnet_{\text{M-G}}(t_d, t_{ins}), Al_{\text{M-G}}(t_d, t_{ins}), SWE_{\text{M-G}}(t_d, t_{ins}), ST_{\text{M-G}}(t_d, t_{ins}),$$
$$SM_{\text{M-G}}(t_d, t_{ins}), C_{\text{M-G}}(t_d, t_{ins}), W_{\text{M-G}}(t_d, t_{ins}), T_{\text{M-G}}(t_d, t_{ins}), Lwd_{\text{M-G}}(t_d, t_{ins})), \tag{8}$$

where $Lnet_{M-G}$, Al_{M-G}, SWE_{M-G}, ST_{M-G}, SM_{M-G}, C_{M-G}, W_{M-G}, T_{M-G} and Lwd_{M-G} are the net longwave radiation, irradiance, snow water equivalent, soil temperature, soil moisture, vegetation canopy water content, wind speed, air temperature and downwelling longwave radiation respectively; and $f_{\text{M-G-Terra-T1}}$ is an RF model based on Terra MODIS data and its corresponding GLDAS data in T1.

As demonstrated in Section 3.2, a high-resolution LST can be represented as a linear/nonlinear mapping of coarse-resolution multidimensional temporal parameters, and similar mapping relationships can be obtained in adjacent moments and periods (Ding et al., 2022). Therefore, $f_{\text{M-G-Terra}}$ can be equally used to estimate the 1-km all-weather LST at the Aqua overpass time. Since Eq. (8) directly establishes a mapping between the coarse resolution reanalysis data and the 1-km LST, $LST_{\text{M-G-Aqua}}$ and $HFC_{\text{cld-M-G-Aqua-T1}}$ may contain systematic errors due to inadequate downscaling. Therefore, a convolutional implementation of a sliding window was used here to reduce the systematic error contained in $HFC_{\text{cld-M-G-Aqua-T1}}$ (Chen et al., 2011; Wu et al., 2015; Zhang et al., 2019).

The schematic diagram of the convolutional implementation of the sliding window is shown in Fig.3. To fully reduce the systematic bias, the size of the sliding window should be slightly larger than a GLDAS pixel (26×26 km^2). According to Zhang et al. (2019, 2021), HFC_{cld} after optimization of M (i.e., HFC_{cld} after eliminating the systematic errors) can be obtained by convolving the HFC_{cld} of the surrounding similar pixels by combining geological factors (e.g., land surface type, spatial distance, and topography). This method is based on the interrelationship of different LSTs: neighbouring HFC_{cld} are correlated at the limited spatial domain. Previous studies have shown that the approaches analogous to the convolutional implementation of sliding windows have a good ability to improve both the accuracy and the image quality of the merged LSTs (Ding et al., 2022; Long et al., 2020; Zhang et al., 2019). Similar pixels (termed as S) need to meet the following criteria: (i) they are within the same sliding window as the target pixel, and (ii) their land cover type does not differ from the target pixel. Therefore, the target pixel itself is also a reference pixel. Eventually, the HFC_{cld} of target pixel can be expressed as:

$$HFC_{\text{cld-M-Aqua-T1}}(t_d, t_{ins}) = \sum_{i=1}^{n} HFC_{\text{cld-S}_i}(t_d, t_{ins}) \cdot w_{S_i}, \tag{9}$$

where n is the number of similar pixels; $HFC_{\text{cld-S}}$ denotes $HFC_{\text{cld-M-Aqua-T1}}$ of the similar pixels; and w_s is the contribution of similar pixels to M, which can be expressed as:

Earth System
Science
Data
Open Access
Discussions

280
$$
\begin{cases}
w_{S_i} = D_{S_i} \cdot H_{S_i} \cdot N_{S_i} \Big/ \left(\sum_n D_{S_i} \cdot H_{S_i} \cdot N_{S_i} \right) \\[2mm]
D_{S_i} = (1/d_{S_i}) \Big/ \sum_{i=1}^{n} 1/d_{S_i} \\[2mm]
d_{S_i} = \sqrt{(x_{S_n} - x_M)^2 + (y_{S_n} - y_M)^2} \\[2mm]
H_{S_i} = \left| DEM_{S_i} - DEM_M \right| \\[2mm]
N_{S_i} = \left| NDVI_{S_i} - NDVI_M \right|
\end{cases}
, \qquad (10)
$$

where D_S, H_S and N_S are the differences between the similar pixels and M in terms of the spatial distance, DEM and NDVI, respectively.
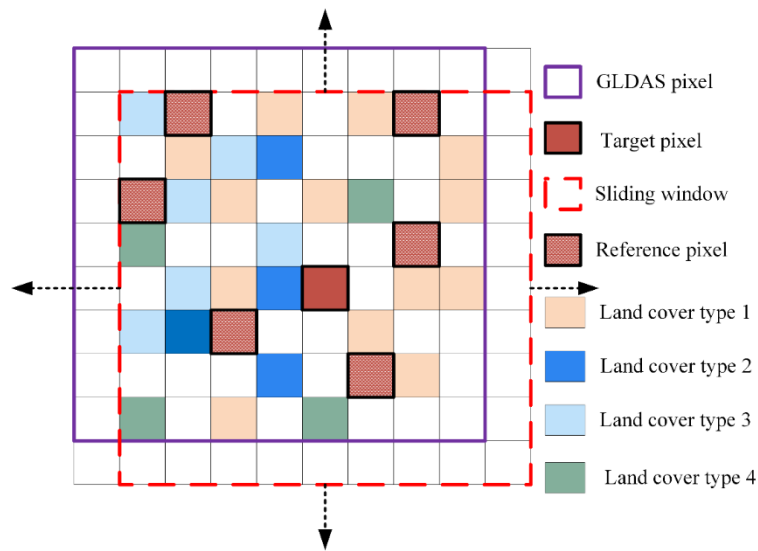
Figure 3: Schematic of HFC_{cld} convolutional optimization.

285 **3.4 Evaluation strategies**

First, the TRIMS LST was compared with LSTs derived from two reanalysis datasets (i.e., GLDAS and the independent ERA5-Land) and retrievals from two different satellite TIR sensor (i.e., MODIS and the independent AATSR). In comparing different LSTs, samples with time differences greater than five minutes were excluded (Freitas et al., 2010; Göttsche et al., 2016; Jiang and Liu, 2014). The quantitative metrics used in comparison analyses include the mean bias deviation (MBD), standard

290 deviation of bias (STD), and coefficient of determination (R^2).

Second, the TRIMS LST was validated under different weather conditions based on *in-situ* LSTs from the ground sites listed in Table I. The three metrics used the mean bias error (MBE), root-mean-square-error (RMSE), and R^2.

Third, the time series angle (TSA), inspired by the spectral angle that is widely used to measure the similarity between spectral curves (Kruse et al., 1993), was used to quantify the similarity of TRIMS LST time series to understand the reliability of the

295 TRIMS LST during the temporal gap of the Aqua/MODIS. The TSA is defined as:

$$\theta = \cos^{-1} \frac{\textbf{LST}_{\text{TRIMS-Aqua}} \cdot \textbf{LST}_{\text{TRIMS-Terra}}}{\left\| \textbf{LST}_{\text{TRIMS-Aqua}} \right\| \cdot \left\| \textbf{LST}_{\text{TRIMS-Terra}} \right\|} , (11)$$

where θ is the TSA (unit: degree); $\textbf{LST}_{\text{TRIMS-Aqua}}$ and $\textbf{LST}_{\text{TRIMS-Terra}}$ are time series of TRIMS-Aqua and TRIMS-Terra LSTs, respectively. From this formula, we know that smaller TSA denotes higher similarity.

Based on the CLCD described in Section 2.1, six subareas with a single land cover type and no land cover change in T1 and
300 T2 (January 1 2000 to January 3 2005) were selected to extract the corresponding TRIMS-Terra and TRIMS-Aqua LST time series. These six subareas were termed A (82.30°N - 83.16°N, 39.63°E - 40.03°E, barren land), B (124.73°N - 125.17°N, 51.51°E - 51.95°E, forest), C (111.84°N -112.30°N, 42.47°E - 42.85°E, grassland), D (100.78°N - 101.53°N, 39.92°E - 40.44°E, barren land), E (98.14°N - 98.61°N, 33.92°E - 34.25°E, grassland), and F (91.73°N - 92.22°N, 31.7°E - 32.01°E, grassland). Then, the TSA was calculated to quantify the similarity between the TRIMS-Terra and TRIMS-Aqua LST time
305 series.

4. Results and discussion

4.1 Comparison of the TRIMS LST with reanalysis data

With the E-RTM method, TRIMS LST products from January 1 2000 to December 31 2021 were generated. The spatial resolution was 1 km. The temporal resolution was four observations per day, which is the same as the overpass time of
310 Terra/MODIS and Aqua/MODIS. Figure 4 shows the daytime TRIMS-Aqua LST on DOY 1, 91, 181, and 271 as examples. For comparison purposes, the GLDAS LST (spatial resolution: 25 km) and ERA5-Land LST (spatial resolution: 10 km) were temporally interpolated to the Aqua overpass time and are also shown in Fig.4.

Figure 4 shows that the TRIMS-Aqua LST has a similar spatial pattern as the GLDAS LST since the latter is an input for the former. Good agreement in the spatial pattern in different seasons can also be observed between TRIMS-Aqua LST and the
315 independent ERA5- Land LST. A careful observation of Fig.4 demonstrates that the TRIMS LST is spatially seamless and its spatial patterns are as expected. Southern China as well as southeast Asia and the south Asian subcontinent in low latitudes are warm in all seasons because of additional absorbed solar radiation; the Tibetan Plateau, with much higher elevation and the regions in high latitudes is much cooler than other regions. In spring (DOY 1), summer (DOY 181), and autumn (DOY 271), northwestern China, where the dominant land cover type is barren land, is much warmer than other regions. Further
320 comparison indicates that TRIMS LST is generally slightly warmer than the GLDAS LST and the ERA5-Land LST. For example, on DOY 1 of 2000, the LSTs are generally below 278 K in the eastern Tibetan Plateau, while the GLDAS LST and the ERA5-Land LST are approximately 3-5 K lower. In the generation scheme of the TRIMS LST, the MODIS LST, which is generally warmer than the LST provided by reanalysis data, is an important input as well as a reference to 'calibrate' the GLDAS LST. This induces the 'merged' TRIMS LST to be warmer than the GLDAS LST as well as the ERA5-Land LST.
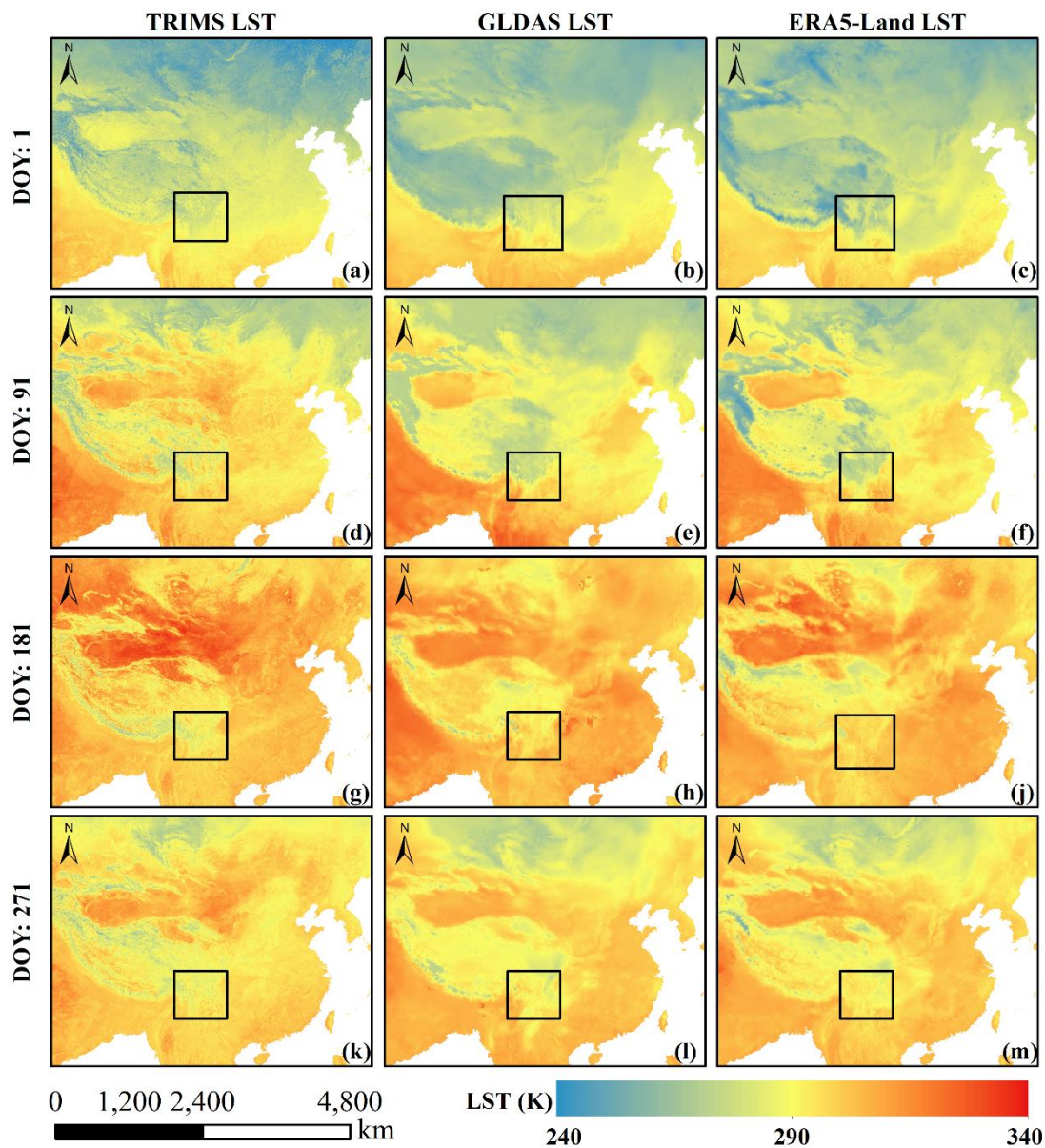
Figure 4: Spatial patterns of the daytime TRIMS-Aqua LST, GLDAS LST, and ERA5-Land LST in 2000.

To further examine the image quality of the TRIMS-Aqua LST, Figure 5 shows the daytime TRIMS-Aqua LST, GLDAS LST, and ERA5-Land LST over the subarea (shown in Fig.4) at the Aqua overpass time in 2000. Due to limited space, Figure 5 only lists the results on DOY 1 (winter) and DOY 181 (summer). Compared with the GLDAS LST and the ERA5-Land LST, the TRIMS LST offers more spatial details because of its much higher spatial resolution. Thus, one can see clear terrain-induced temperature variations. Furthermore, Figure 5 shows that no evident spatial discontinuities exist in the TRIMS LST, indicating the E-RTM method performs satisfactorily in addressing the spatial scale mismatch between the MODIS LST and GLDAS LST (Zhang et al., 2021).
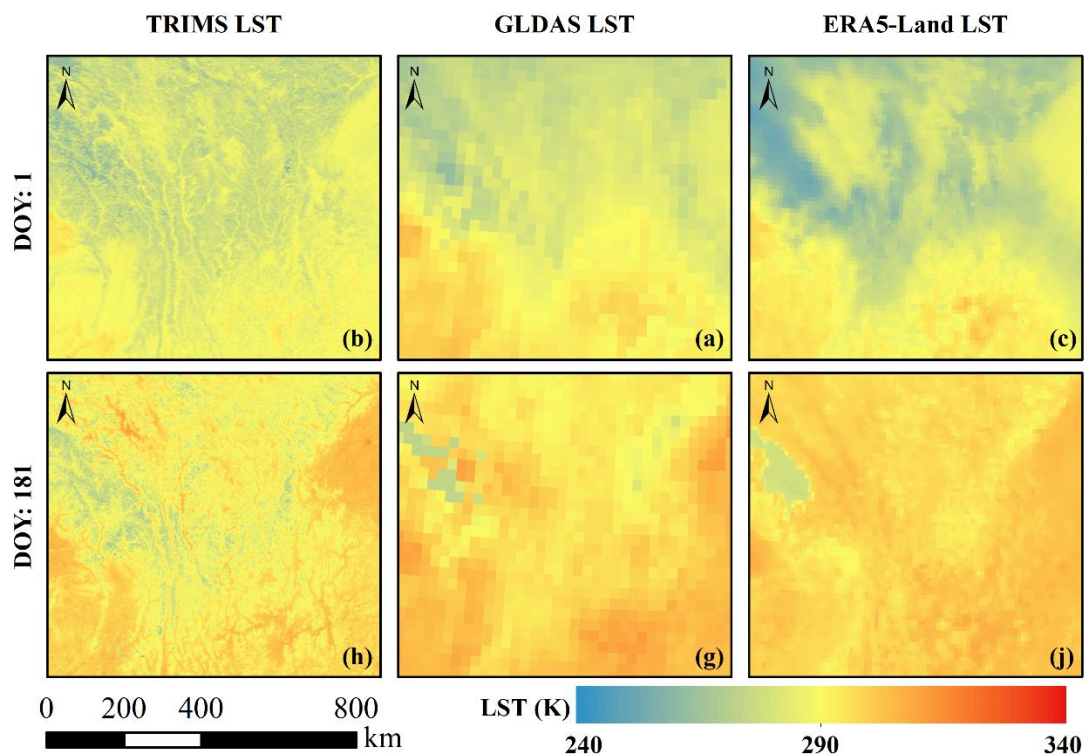
Figure 5: The daytime TRIMS-Aqua LST, GLDAS LST, and ERA5-Land LST over the subarea (shown in Fig.4) in 2000.

4.2 Comparison of the TRIMS LST with satellite TIR LST products

The daily TRIMS LST was compared with the independent ENVISAT/AATSR LST (from 2004 to 2012) and the Terra/Aqua MODIS LST (from 2000 to 2021 for Terra and from 2002 to 2021 for Aqua). Note that the AATSR and MODIS only have clear-sky LSTs. The density plots are shown in Fig.6. To facilitate the data processing and presentation, 1%/1‰ matched TRIMS-AATSR/MODIS pairs were randomly extracted. Figure 6 indicates good consistency between the TRIMS LST and AATSR/MODIS LST. Compared with AATSR, the overall MBD/STD values of TRIMS were 0.37 K/1.55 K and -0.44 K/1.22 K for daytime and nighttime, respectively; compared with MODIS, the overall MBD/STD values were 0.09 K/1.45 K and -0.03 K/1.17 K for daytime and nighttime, respectively. Figure.6 also shows that better agreements are observed during nighttime because of lower thermal heterogeneity.

16
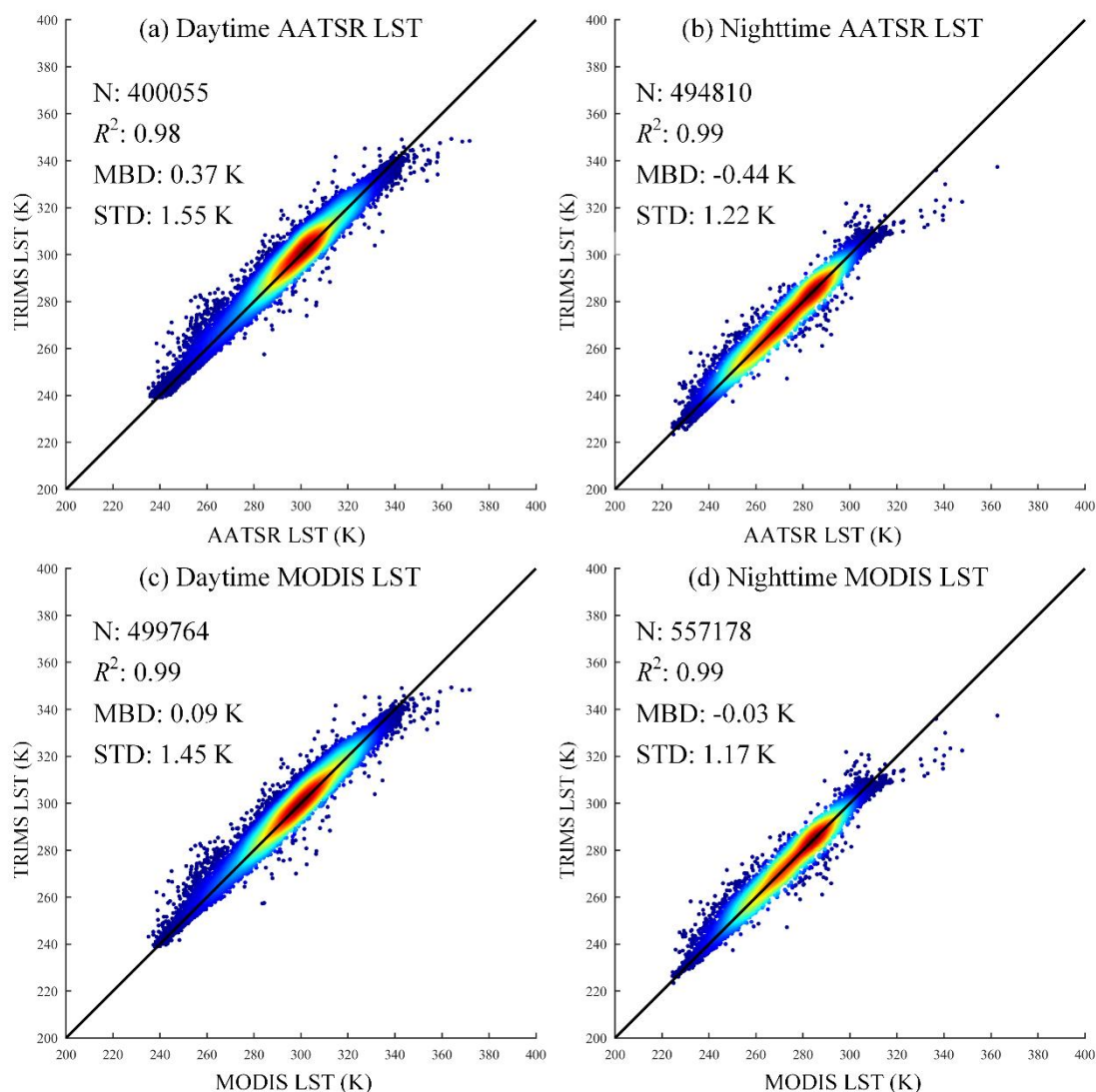
Figure 6: Density plots between the TRIMS LST and satellite TIR LST.

To further examine the deviation of the TRIMS LST from AATSR/MODIS LST, the MBD and STD values were calculated for each day. Figure 7 shows the corresponding histograms. For AATSR, the daily daytime MBD and STD were mainly
350   concentrated in the ranges of 0 K - 0.60 K and 1.05 K - 1.15 K, respectively; the daily nighttime MBD and STD were mainly concentrated in the ranges of -0.40 K to 1.0 K and 0.75 K to 1.15 K, respectively. The positive deviation and negative deviation were consistent with those in Fig.6(a) and Fig.6(b). For the MODIS case, the daytime MBD was concentrated between -0.6 K and 1.0 K, and STD was concentrated between 1.0 K and 2.50 K; the nighttime MBD was concentrated between -0.6 K and 0.3 K and STD was concentrated between 0.9 K and 1.50 K. As shown above, it should be concluded that the daily differences
355   between the long-term TRIMS LST and AATSR/MODIS LST remain stable.
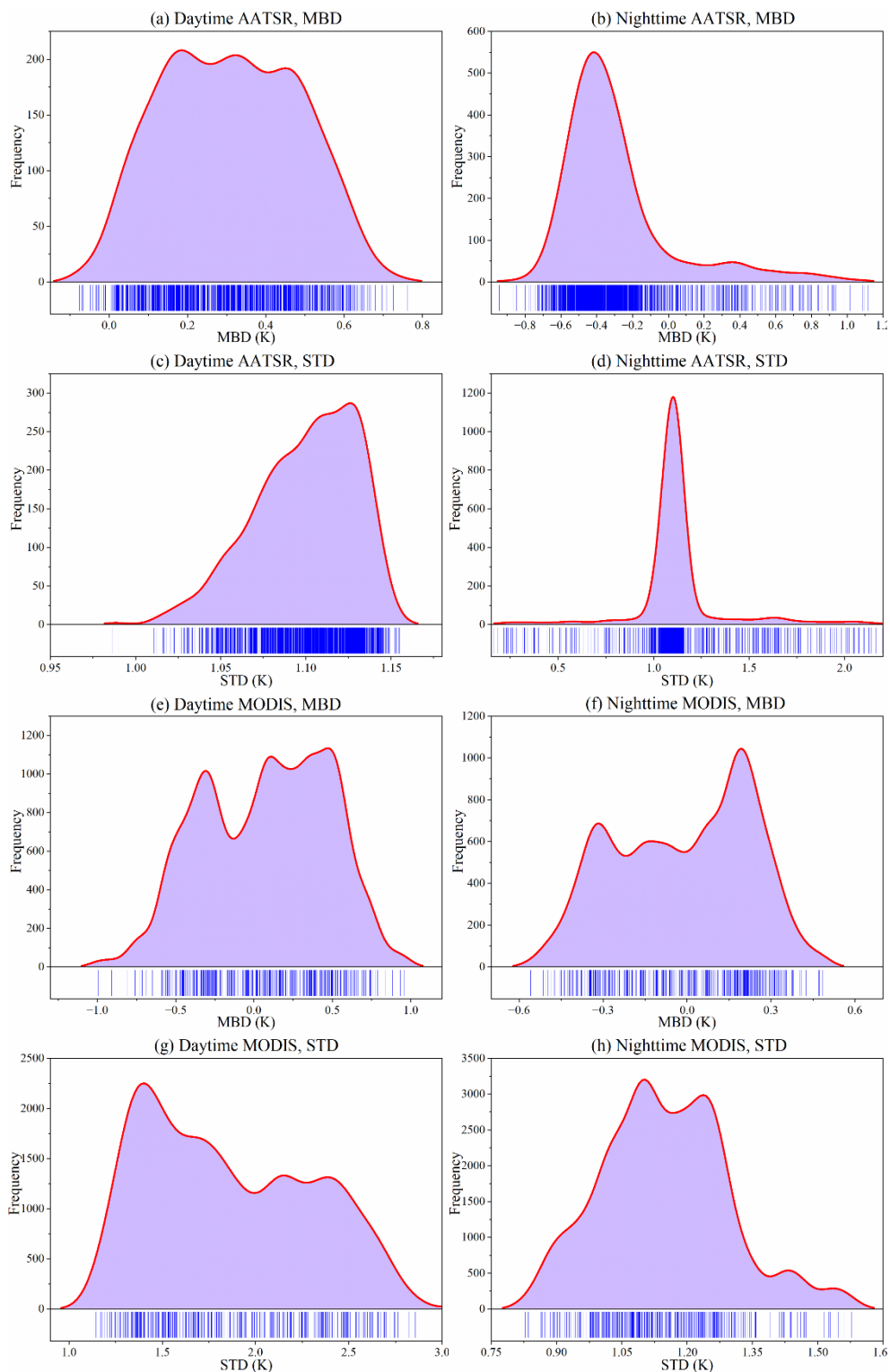
Figure 7: Histograms of the MBD and STD to compare the TRIMS LST and satellite TIR LST.

4.3 Validation results against *in-situ* LST

The TRIMS LST was quantitative validated against the *in-situ* LST. Remove anomalies caused by transient environmental
360 factors based on 3σ (standard deviation) filtering (Göttsche et al., 2016; Yang et al., 2020). Due to limited space, the results
for all sites are not shown in the main text, and can be found in Table B1 and B2. The nineteen ground sites were divided into
four groups according to locations and land cover types (Group I: ARO, D105, DSL, EBA, MQU; Group II: DET, GAZ, GOB,
HZZ, SSW; Group III: DAM, DXI, GUT, HLA, TYU; Group IV: CBS, DHS, QYZ, SDQ). Table II and Table III show the
validation results of TRIMS LST against the *in-situ* LST under different weather conditions. In addition, the validation results
365 of the clear-sky MODIS LST are provided for comparison.

Table II: R^2, MBE, and RMSE of the daytime validation for different groups.

Group	Land cover type	Condition	Amounts	TRIMS LST			MODIS LST		
				MBE (K)	RMSE (K)	R^2	MBE (K)	RMSE (K)	R^2
I	Grassland	Clear-sky	5370	0.26	2.15	0.95	0.61	2.37	0.95
		Cloudy	6972	0.41	2.18	0.96			
II	Desert or bare land	Clear-sky	5930	0.46	2.30	0.98	0.79	2.53	0.98
		Cloudy	5698	0.43	2.26	0.98			
III	Farmland	Clear-sky	5738	0.02	2.11	0.97	-0.21	2.52	0.95
		Cloudy	7570	0.04	2.11	0.97			
IV	Forest	Clear-sky	3170	0.55	2.46	0.97	0.72	2.38	0.98
		Cloudy	3655	0.68	2.27	0.98			

Table III: R^2, MBE, and RMSE of the nighttime validation for different groups.

Group	Land cover type	Condition	Amounts	TRIMS LST			MODIS LST		
				MBE (K)	RMSE (K)	R^2	MBE (K)	RMSE (K)	R^2
I	Grassland	Clear-sky	8175	-0.70	1.65	0.98	-0.99	1.69	0.98
		Cloudy	5254	-0.13	1.64	0.97			
II	Desert or bare land	Clear-sky	6095	-0.64	1.43	0.99	-0.67	1.53	0.99
		Cloudy	5244	-1.17	1.85	0.99			
III	Farmland	Clear-sky	5314	-0.83	1.76	0.98	-0.75	1.60	0.98
		Cloudy	7243	-0.60	1.74	0.98			
IV	Forest	Clear-sky	2800	-0.98	1.92	0.98	-0.97	2.09	0.98

		Cloudy	3332	-0.94	1.90	0.99			

370   Under clear-sky conditions, the TRIMS LST had an accuracy close to that of the MODIS LST as shown in Table II and Table III. The MBE of the TRIMS LST ranged from -0.98 K to 0.68 K and the RMSE was 1.43 K to 2.46 K. The RMSE of the TRIMS LST under clear-sky conditions was lower than that of the MODIS LST, except for Group IV. The RMSEs of the MODIS LST were reduced by 0.22 K (Group I), 0.23 K (Group II), and 0.41 K (Group III) respectively. The nighttime results were generally better than the daytime results, with an average RMSE of 1.74 K. The R^2 of the TRIMS LST for the four groups

375   of sites were higher than 0.95 under clear-sky conditions, indicating that the TRIMS LST was in good agreement with the *in-situ* LST. The improved accuracy of the TRIMS LST may be due to the reduction of the systematic bias of the original MODIS LST in the E-RTM method by extracting the LFC and HFC (Ding et al., 2022).

For TRIMS LST under ckoudy conditions, the accuracy is marginally below that under clear-sky conditions, and the overall RMSE increased by 0.35 K. For the four groups of sites, the MBE values of TRIMS LST were -0.13 K (Group I), -1.17 K

380   (Group II), -0.60 K (Group III) and -0.94 K (Group IV), revealing that the TRIMS LST was underestimated under cloudy conditions. According to the parameterization scheme of the E-RTM method, the accuracy of the estimated HFC_{cld} under cloudy conditions is affected by the GLDAS LST, which has a negative deviation from the MODIS LST as shown in Section 4.1. While the GLDAS LST is bias-corrected, uncertainty may still exist, which are ultimately detrimental to the accurate recovery of the LST for the cloud-contaminated region. Overall, the validation results indicate that TRIMS LST has good

385   accuracy under cloudy conditions as well as under clear-sky conditions..

For ground sites in Group III with a dominant land cover type of desert or barren land, the nighttime validation shows that the TRIMS-Aqua LST was systematically underestimated, with an MBE of -1.17 K to -0.64 K. After checking the calculated μ_{REP}, we believe the spatial scale mismatch between the ground site and the pixel is not the main cause of the systematic underestimation. Further examination shows that the clear-sky MODIS LST is significantly underestimated: the MBEs of

390   Aqua/MODIS LST were -1.88 K, -1.03 K, -1.33 K and -0.60 K for GOB, HZZ, SSW and GAZ, respectively. Such a cold bias in arid and semiarid regions was also been reported by Li et al. (2019) for the MYD11 LST product. The above results indicate that hat for TRIMS LST, the accuracy is largely dependent on the MODIS LST used.

4.4 Quantification of the similarity between the TRIMS-Aqua LST and TRIMS-Terra LST time series during the temporal gaps

395   The quantification results are shown in Fig.8. Overall, the trends in the time series of TRIMS-Terra and TRIMS-Aqua LST are very consistent, and they generally have a high degree of similarity. The daytime time series show that the TRIMS-Aqua LST was generally higher than the TRIMS-Terra LST, while the opposite was observed for the nighttime. I In particular, for subareas E and F, the TRIMS-Aqua LST showed a significant systematic deviation from the TRIMS-Terra LST during nighttime. The distribution of the curves in Fig.8 reveals that the daytime LST time series had more large fluctuations, while

400   the nighttime variation was more subdued. The TSA was lower at nighttime than daytime, indicating that the time series

Earth System
Science
Data
Open Access
Discussions

similarity between the TRIMS-Aqua LST and the TRIMS-Terra LST is higher at nighttime. In addition, the TRIMS-Terra and TRIMS-Aqua LSTs were slightly more similar in the T1 than in T2 among these six regions. This situation is as expected, since the TRIMS-Aqua LST in T1 is derived from a mapping created by the data at the Terra overpass time. The differences in the TSA between T1 and T2 ranged from 0.0080 to 0.0710. The mean differences were 0.0465 (daytime) and

405   0.0433(nighttime). The above results indicate that the similarity of the LST time series of T1 and T2 is relatively close. This finding demonstrates that the difference between TRIMS LST at the Aqua and Terra overpass times is stable in T1.
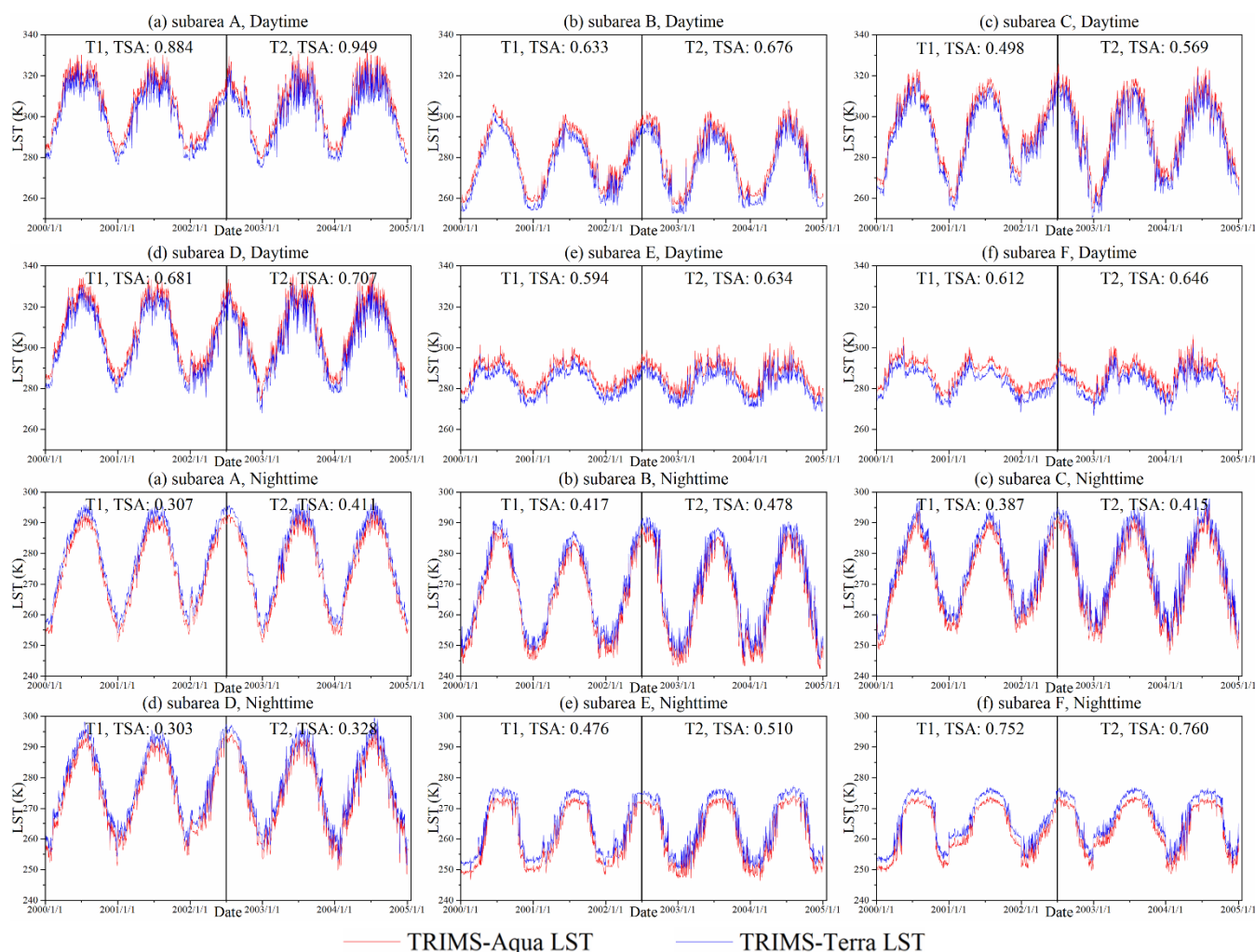
Figure 8: TRIMS-Terra and TRIMS-Aqua LSTs from January 1, 2000 to January 3, 2005 and statistics of the time series similarity.

4.4 Literature-reported applications of the TRIMS LST

410   TRIMS LSTs have already been utilized by the scientific communities in different applications (Fig.9). A literature survey indicates that there have been 28 related papers published by journals (as of January 13, 2023), including leading journals such as Remote Sensing of Environment, Agricultural Water Management, and Science of the Total Environment. Typical

applications include the estimation of soil moisture and surface evapotranspiration as well as modelling of urban heat is land and urban thermal environment. A few typical applications are listed below.
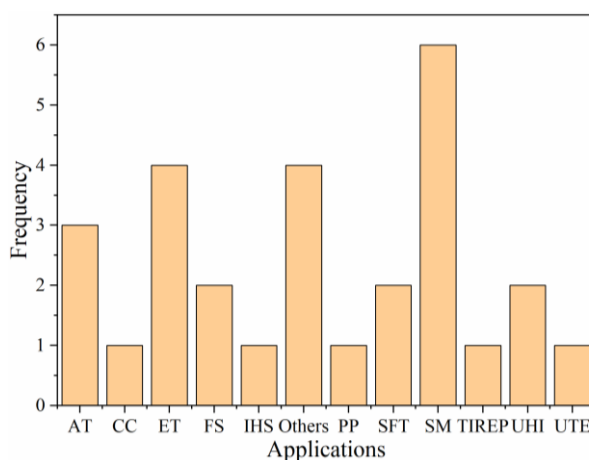
415

Figure 9: Statistics of applications based on TRIMS LST (AT: Air temperature; CC: Climate change; ET: Evapotranspiration; FS: Frozen soil; IHS: Industrial heat sources; Others: Active layer thickness, Lake Area, Land desertification, and LST downscaling; PP: Plant Phenology; SFT: Soil freeze/thaw; SM: Soil moisture; TIREP: Thermal Infrared Earthquake Prediction; UHI: Urban heat island; UTE: Urban Thermal Environment.).

420 Satellite TIR LSTs are an important input data for obtaining SM estimates with high resolution and high spatial coverage. However, most satellite TIR LST products can only be used under clear-sky conditions. The availability of all-sky LST products provides an important opportunity to obtain SMs with spatial seamlessness. Zhang et al. (2023) combined the use of ERA5-Land and TRIMS LST for the fine-scale assessment of soil moisture in in China. They used the model based on 0.1° ERA5 Land and SSM data for 1-km TRIMS LST, and finally obtained a daily/1-km SM dataset with satisfactory accuracy.

425 Benefiting from the effective recovery of LST under cloudy conditions, this SM dataset has quasi-full spatial coverage. In addition, Hu et al. (2022) also used the TRIMS LST as input data to construct a soil moisture downscaling model for the Tibetan Plateau. The TRIMS LST was found to successfully overcome the challenges of satellite TIR remote sensing detection due to temporal/spatial gaps and false detections due to clouds and topography. Based on the downscaled soil moisture, they further published the daily 0.05°×0.05° land surface soil moisture dataset of the Qilian Mountain area (northern and

430 northwestern Tibetan Plateau) from 2019-2021 (SMHiRes, V2) (Hu et al., 2022; Qu et al., 2021; Chai et al., 2021, 2022a, b). LST can also be used to investigate the soil freeze/thaw cycles. Li et al. (2023) used the TRIMS LST to obtain thawing degree days and freezing degree days to calculate the soil thermal conductivity and improved the output of the temperature at the top of the permafrost model. Due to the characteristics of TRIMS LST: high spatial and temporal resolution, the above two metrics can be easily obtained on a spatial scale of 1 km. In addition, the TRIMS LST was also used to evaluate the impact of the LST

435 on the classification accuracy on different remote-sensed or model-based freeze/thaw datasets (Li et al., 2022).

Based on the TRIMS LST, Li et al. (2021b) investigated the spatial and temporal variations of surface UHI (SUHI) intensity (SUHII). The positive performance of the TRIMS LST in obtaining the LST under cloudy conditions enabled the examination of the SUHI intensity of 305 Chinese cities, especially the cities located in southern China, where clouds frequently appear.

440 Furthermore, Liao et al. (2022) quantified the clear-sky bias of the SUHI intensity in using the MODIS LST based on the TRIMS LST. They emphasized the importance of investigating the SUHI phenomenon under cloudy conditions.

5. Data availability

TRIMS LST is available for free and easy access through TPDC: https://doi.org/10.11888/Meteoro.tpdc.271252 (Zhou et al., 2021).

6. Conclusions

445 A long-term 1-km daily all-weather LST dataset is the basis for supporting many applications related to land surface process and climate change. Although some all-weather LST datasets have been released, especially in the last two years, users still lack such data for the period of 2000-2002, during which the MODIS LST is not available. In this study, we report a daily 1-km all-weather LST dataset for the Chinese landmass and surrounding areas – TRIMS LST. In contrast to many all-weather LST products, the TRIMS LST begins from the first day of the new millennium (i.e., January 1, 2000).

450 TRIMS LST is produced based on the E-RTM method. The primary input resources are the Terra/Aqua MODIS LST and GLDAS LST. The TRIMS LST was comprehensively evaluated thoroughly from four aspects, including comparison with satellite and reanalysis LSTs, validation against the *in-situ* LSTs, and similarity quantification for the TRIMS-Terra and TRIMS-Aqua LST time series. The results indicate that the TRIMS LST agrees well with the original MODIS and GLDAS LSTs and the independent ERA5 and AATSR LSTs, but with more spatial details and better spatio-temporal completeness.

455 Validation of TRIMS LST using the *in-situ* LST at 19 ground sites showed that the MBE was -2.26 K to 1.73 K and the RMSE was 0.80 K to 3.68 K, with slightly better accuracy than the MODIS LST and no obvious difference under different weather conditions.

The TRIMS LST has been released to the scientific communities. A series of applications, such as soil moisture estimation/downscaling, surface evapotranspiration estimation, and urban heat island (UHI) modelling, have been reported.

460 The TRIMS LST was found to successfully address the cloud contamination of satellite TIR LST and with good accuracy, long time series, and spatio-temporal completeness. The TRIMS LST will be continuously updated to satisfy the latest requirements of users.

Appendix A: List of abbreviations

Land surface temperature	LST
the Thermal and Reanalysis Integrating Moderate-resolution Spatial- seamless LST	TRIMS LST
the Enhanced Reanalysis and Thermal infrared remote sensing Merging method	E-RTM
Thermal infrared remote sensing	TIR
Moderate Resolution Imaging Spectroradiometer	MODIS
Visible infrared Imaging Radiometer	VIIRS
Passive microwave	(PMW)
Advanced Microwave Scanning Radiometer 2	AMSR2
Normalized Difference Vegetation Index	NDVI
Normalized Difference Snow Index	NDSI
Advanced Synthetic Aperture Radar	AATSR
Shuttle Radar Topography Mission Digital Elevation Model data	SRTM DEM
30-m yearly China land cover dataset (2000-2015)	CLCD
Global Land Data Assimilation System assimilation	GLDAS
the Goddard Earth Sciences Data and Information Services Center	GES DISC
Field-of-view	FOV
Mean bias deviation	MBD
Standard deviation of bias/	STD
Mean bias error	MBE
Root mean square error	RMSE
Time series angle	TSA
Day of the year	DOY
Random-Forest based Spatio-Temporal Merging approach	RFSTM
Time-Sequential LST based Reconstruction approach	TSETR
Urban heat island	UHI
Soil moisture	SM
Evapotranspiration	ET
Surface UHI	SUHI
Surface UHI intensity	SUHII

465

Appendix B: R^2, MBE, and RMSE from validation results of the TRIMS LST and the MODIS LST with the *in-situ* LST

Table B1: R^2, MBE, and RMSE from validation results of the daytime TRIMS LST and MODIS LST with *in-situ* LST

Site	Condition	Sample size		TRIMS LST				MODIS LST			
				MBE (K)		RMSE (K)		MBE (K)		RMSE (K)	
		MOD	MYD	MOD	MYD	MOD	MYD	MOD	MYD	MOD	MYD
ARO	clear	1418	1029	0.43	0.48	2.30	1.87	0.74	0.57	2.95	2.38
	cloudy	1228	1541	0.33	0.61	2.04	1.95	—	—	—	—
DAM	clear	1363	1297	0.97	0.26	1.92	1.98	0.98	0.27	2.31	2.50
	cloudy	1432	1492	0.67	0.18	1.81	2.07	—	—	—	—
DET	clear	1191	1180	1.73	1.45	2.45	2.49	1.73	1.88	2.70	2.70
	cloudy	830	896	1.70	1.45	2.67	2.43	—	—	—	—
DSL	clear	1109	814	-0.01	-0.33	1.82	1.72	0.00	-0.32	2.38	2.28
	cloudy	1198	1144	-0.01	0.48	1.91	1.65	—	—	—	—
EBA	clear	410	289	0.63	0.59	2.06	1.90	0.65	0.53	2.38	2.31
	cloudy	472	580	0.74	0.61	2.01	1.80	—	—	—	—
GOB	clear	363	350	-0.58	-1.88	1.73	2.41	-0.61	-1.89	2.25	2.74
	cloudy	368	390	-0.96	-1.65	1.72	2.71	—	—	—	—
HZZ	clear	1046	975	1.06	-1.03	1.84	2.06	1.05	-1.04	2.40	3.14
	cloudy	1219	1354	0.59	-0.66	1.78	2.05	—	—	—	—
SDQ	clear	1507	1466	0.82	0.23	2.57	2.05	0.81	0.39	3.16	2.57
	cloudy	1147	1132	0.86	0.37	2.49	2.23	—	—	—	—
SSW	clear	191	174	-0.42	-1.33	2.09	2.08	-0.43	-1.35	3.10	2.51
	cloudy	194	203	-1.23	-1.77	2.36	2.45	—	—	—	—
HLA	clear	1121	946	-0.79	-0.85	2.30	2.18	-0.74	-0.71	2.76	2.60
	cloudy	1084	1159	-0.68	-0.75	2.68	1.81	—	—	—	—
D105	clear	92	44	1.61	1.28	3.68	2.53	1.36	0.67	4.09	2.71
	cloudy	178	138	1.29	0.61	3.94	2.74	—	—	—	—
GAZ	clear	220	240	0.74	-0.60	2.12	2.17	0.47	-0.55	2.37	2.82

Site	Condition										
	cloudy	89	157	1.15	-0.85	2.11	1.96	—	—	—	—
CBS	clear	54	56	0.49	1.38	2.41	3.41	0.85	1.49	2.39	3.43
	cloudy	220	262	0.76	1.59	2.42	3.43	—	—	—	—
DXI	clear	246	226	0.83	0.30	2.13	1.79	0.80	0.28	2.33	2.00
	cloudy	547	562	0.81	0.54	2.19	1.79	—	—	—	—
DHS	clear	23	21	0.38	0.77	1.37	1.53	0.30	0.74	0.74	1.18
	cloudy	292	299	0.42	0.47	1.51	1.22	—	—	—	—
MQU	clear	101	64	0.15	-1.50	2.43	2.85	0.12	-1.47	3.05	3.13
	cloudy	77	117	0.05	-1.35	2.27	2.99	—	—	—	—
GUT	clear	69	63	-0.22	0.02	2.10	2.25	-0.29	-0.07	2.20	2.25
	cloudy	310	303	-0.28	0.60	1.83	2.22	—	—	—	—
QYZ	clear	26	19	0.95	1.01	3.00	3.17	0.73	0.90	2.35	2.14
	cloudy	139	177	0.71	0.91	2.71	3.35	—	—	—	—
TYU	clear	211	196	0.37	-0.88	2.56	2.14	0.31	-0.90	3.01	2.63
	cloudy	333	348	0.19	-0.58	2.63	2.03	—	—	—	—

470 Table B2: R^2, MBE, and RMSE from validation results of the nighttime TRIMS LST and MODIS LST with the *in-situ* LST.

Site	Condition	Sample size		TRIMS LST				MODIS LST			
				MBE (K)		RMSE (K)		MBE (K)		RMSE (K)	
		MOD	MYD	MOD	MYD	MOD	MYD	MOD	MYD	MOD	MYD
ARO	clear	1617	1757	-0.72	-0.53	1.87	1.67	-0.70	-0.60	2.09	1.90
	cloudy	1196	1078	-0.68	-0.63	1.62	1.76	—	—	—	—
DAM	clear	853	973	-0.80	-0.58	2.14	1.70	-0.82	-0.81	2.23	1.87
	cloudy	1643	1673	-0.86	-0.52	1.98	1.64	—	—	—	—
DET	clear	1325	1476	-0.08	0.17	0.83	0.90	-0.08	0.16	0.86	0.97
	cloudy	679	630	0.42	-0.23	0.80	0.83	—	—	—	—
DSL	clear	1109	1646	-0.90	-0.84	1.82	1.50	-0.45	-0.42	1.92	1.78
	cloudy	1198	797	-1.13	0.44	1.91	1.24	—	—	—	—
EBA	clear	566	621	-0.61	-0.60	1.65	2.00	-0.58	-0.64	1.77	2.19
	cloudy	443	404	-0.55	-0.64	1.56	1.68	—	—	—	—

GOB	clear	467	381	-1.60	-1.65	2.05	1.93	-1.62	-1.65	1.96	1.96
	cloudy	376	321	-2.04	-1.51	2.26	1.79	—	—	—	—
HZZ	clear	772	944	-1.29	-0.94	1.86	1.46	-1.28	-0.93	2.03	1.65
	cloudy	1348	1296	-1.77	-1.36	2.32	1.86	—	—	—	—
SDQ	clear	1557	1286	-0.79	-0.94	2.61	2.33	-1.02	-0.93	2.68	2.44
	cloudy	1112	981	-1.06	-0.94	2.70	2.15	—	—	—	—
SSW	clear	172	164	-2.26	-1.87	2.53	2.11	-2.27	-1.86	2.59	2.15
	cloudy	195	190	-1.95	-1.79	2.29	2.00	—	—	—	—
HLA	clear	1042	1038	-0.82	-0.73	2.24	1.61	-0.85	-0.73	2.34	1.75
	cloudy	1066	989	-0.85	-0.87	2.24	1.55	—	—	—	—
D105	clear	131	167	-1.07	-0.92	2.39	2.57	-1.05	-1.12	2.58	2.69
	cloudy	95	121	-1.05	-1.10	2.81	2.74	—	—	—	—
GAZ	clear	289	265	-0.63	-0.68	1.85	1.35	-0.68	-0.57	1.90	1.39
	cloudy	124	86	-0.75	-0.69	1.80	1.32	—	—	—	—
CBS	clear	95	98	-1.07	-0.55	2.81	2.21	-1.00	-0.50	2.79	2.26
	cloudy	190	208	-1.00	-0.33	3.31	2.37	—	—	—	—
DXI	clear	334	349	-1.10	-1.45	3.43	3.06	-1.65	-1.44	3.51	3.13
	cloudy	454	446	-1.15	-1.42	3.77	2.58	—	—	—	—
DHS	clear	53	53	-0.82	-0.74	1.97	2.31	-0.74	-0.89	1.83	2.22
	cloudy	264	262	-0.81	-0.89	2.35	2.30	—	—	—	—
MQU	clear	85	81	0.68	0.78	2.23	2.41	0.76	0.70	2.16	2.40
	cloudy	105	90	0.81	0.76	2.32	2.53	—	—	—	—
GUT	clear	122	126	-0.90	-0.76	2.14	1.80	-0.94	-0.78	2.19	1.81
	cloudy	237	230	-0.93	-0.70	2.49	1.78	—	—	—	—
QYZ	clear	32	28	-0.90	-0.91	3.00	2.09	-1.16	-0.80	2.62	1.88
	cloudy	145	175	-1.13	-0.88	3.49	2.37	—	—	—	—
TYU	clear	235	242	-1.12	-0.78	2.65	2.26	-0.94	-0.75	2.69	2.25
	cloudy	258	273	-1.13	-0.79	2.91	2.37	—	—	—	—

Author contribution

WBT implemented the E-RTM method, completed the thorough evaluation and wrote the earliest version of the manuscript, JZ examined the entire process of generation and release and provided necessary guidance, JM helped to obtain the measured 475 data and provided the method to quantify the spatial representation, and XDZ proposed the original RTM method. All co-authors contributed to the writing and carefully reviewed and revised the manuscript.

Competing interests

The authors declare that they have no conflict of interest.

Acknowledgements

References

Aguilar-Lome, J., Espinoza-Villar, R., Espinoza, J.-C., Rojas-Acuna, J., Leo Willems, B., and Leyva-Molina, W.-M.: Elevation-dependent warming of land surface temperatures in the Andes assessed using MODIS LST time series (2000-2017), 490 Int. J. Appl. Earth Obs. Geoinformation, 77, 119–128, https://doi.org/10.1016/j.jag.2018.12.013, 2019.

Alexander, C.: Normalised difference spectral indices and urban land cover as indicators of land surface temperature (LST), Int. J. Appl. Earth Obs. Geoinformation, 86, 102013, https://doi.org/10.1016/j.jag.2019.102013, 2020.

Anderson, M. C., Kustas, W. P., Norman, J. M., Hain, C. R., Mecikalski, J. R., Schultz, L., González-Dugo, M. P., Cammalleri, C., d'Urso, G., Pimstein, A., and Gao, F.: Mapping daily evapotranspiration at field to continental scales using geostationary 495 and polar orbiting satellite imagery, Hydrol. Earth Syst. Sci., 15, 223–239, https://doi.org/10.5194/hess-15-223-2011, 2011.

Bechtel, B.: A New Global Climatology of Annual Land Surface Temperature, Remote Sens., 7, 2850–2870, https://doi.org/10.3390/rs70302850, 2015.

Chai, L., Zhu, Z., and Liu, S.: Daily 0.05°×0.05° land surface soil moisture dataset of Qilian Mountain area (2019,SMHiRes,V2), edited by: National Tibetan Plateau Data Center, Natl. Tibet. Plateau Data Cent., 2021.

500   Chai, L., Zhu, Z., and Liu, S.: Daily 0.05°×0.05° land surface soil moisture dataset of Qilian Mountain area
(2020,SMHiRes,V2), edited by: National Tibetan Plateau Data Center, Natl. Tibet. Plateau Data Cent.,
https://doi.org/10.11888/Terre.tpdc.272375, 2022a.

Chai, L., Zhu, Z., and Liu, S.: Daily 0.05°×0.05° land surface soil moisture dataset of Qilian Mountain area
(2021,SMHiRes,V2), edited by: National Tibetan Plateau Data Center, Natl. Tibet. Plateau Data Cent.,
505   https://doi.org/10.11888/Terre.tpdc.272375, 2022b.

Che, T., Li, X., Liu, S., Li, H., Xu, Z., Tan, J., Zhang, Y., Ren, Z., Xiao, L., Deng, J., Jin, R., Ma, M., Wang, J., and Yang, X.:
Integrated hydrometeorological, snow and frozen-ground observations in the alpine region of the Heihe River Basin, China,
Earth Syst. Sci. Data, 11, 1483–1499, https://doi.org/10.5194/essd-11-1483-2019, 2019.

Chen, C., Park, T., Wang, X., Piao, S., Xu, B., Chaturvedi, R. K., Fuchs, R., Brovkin, V., Ciais, P., Fensholt, R., Tømmervik,
510   H., Bala, G., Zhu, Z., Nemani, R. R., and Myneni, R. B.: China and India lead in greening of the world through land-use
management, Nat. Sustain., 2, 122–129, https://doi.org/10.1038/s41893-019-0220-7, 2019a.

Chen, S., Chen, X., Chen, W., Su, Y., and Li, D.: A simple retrieval method of land surface temperature from AMSR-E passive
microwave data—A case study over Southern China during the strong snow disaster of 2008, Int. J. Appl. Earth Obs.
Geoinformation, 13, 140–151, 2011.

515   Chen, Y., Chen, W., Su, Q., Luo, F., Sparrow, S., Wallom, D., Tian, F., Dong, B., Tett, S. F. B., and Lott, F. C.: Anthropogenic
Warming has Substantially Increased the Likelihood of July 2017–Like Heat Waves over Central Eastern China, Bull. Am.
Meteorol. Soc., 100, S91–S95, https://doi.org/10.1175/BAMS-D-18-0087.1, 2019b.

Coops, N. C., Duro, D. C., Wulder, M. A., and Han, T.: Estimating afternoon MODIS land surface temperatures (LST) based
on morning MODIS overpass, location and elevation information, Int. J. Remote Sens., 28, 2391–2396,
520   https://doi.org/10.1080/01431160701294653, 2007.

Ding, L., Zhou, J., Li, Z.-L., Ma, J., Shi, C., Sun, S., and Wang, Z.: Reconstruction of Hourly All-Weather Land Surface
Temperature by Integrating Reanalysis Data and Thermal Infrared Data From Geostationary Satellites (RTG), IEEE Trans.
Geosci. Remote Sens., 60, 1–17, https://doi.org/10.1109/TGRS.2022.3227074, 2022.

Duan, S., Li, Z., and Leng, P.: A framework for the retrieval of all-weather land surface temperature at a high spatial resolution
525   from polar-orbiting thermal infrared and passive microwave data, Remote Sens. Environ., 195, 107–117,
https://doi.org/10.1016/j.rse.2017.04.008, 2017.

Freitas, S. C., Trigo, I. F., Bioucas-Dias, J. M., and Gottsche, F.-M.: Quantifying the Uncertainty of Land Surface Temperature
Retrievals From SEVIRI/Meteosat, IEEE Trans. Geosci. Remote Sens., 48, 523–534,
https://doi.org/10.1109/TGRS.2009.2027697, 2010.

530   Göttsche, F.-M., Olesen, F.-S., Trigo, I. F., Bork-Unkelbach, A., and Martin, M. A.: Long Term Validation of Land Surface
Temperature Retrieved from MSG/SEVIRI with Continuous in-Situ Measurements in Africa, Remote Sens., 8, 410,
https://doi.org/10.3390/rs8050410, 2016.

Guo, A., Liu, S., Zhu, Z., Xu, Z., Xiao, Q., Ju, Q., Zhang, Y., and Yang, X.: Impact of Lake/Reservoir Expansion and Shrinkage
on Energy and Water Vapor Fluxes in the Surrounding Area, J. Geophys. Res.-Atmospheres, 125, e2020JD032833,
535   https://doi.org/10.1029/2020JD032833, 2020.

Holmes, T. R. H., De Jeu, R. a. M., Owe, M., and Dolman, A. J.: Land surface temperature from Ka band (37 GHz) passive
microwave observations, J. Geophys. Res. Atmospheres, 114, https://doi.org/10.1029/2008JD010257, 2009.

Hong, F., Zhan, W., Göttsche, F.-M., Liu, Z., Dong, P., Fu, H., Huang, F., and Zhang, X.: A global dataset of spatiotemporally seamless daily mean land surface temperatures: generation, validation, and analysis, Earth Syst. Sci. Data, 14, 3091–3113, 540   https://doi.org/10.5194/essd-14-3091-2022, 2022.

Hu, Z., Chai, L., Crow, W. T., Liu, S., Zhu, Z., Zhou, J., Qu, Y., Liu, J., Yang, S., and Lu, Z.: Applying a Wavelet Transform Technique to Optimize General Fitting Models for SM Analysis: A Case Study in Downscaling over the Qinghai-Tibet Plateau, Remote Sens., 14, 3063, https://doi.org/10.3390/rs14133063, 2022.

Jia, A., Ma, H., Liang, S., and Wang, D.: Cloudy-sky land surface temperature from VIIRS and MODIS satellite data using a 545   surface energy balance-based method, Remote Sens. Environ., 263, 112566, https://doi.org/10.1016/j.rse.2021.112566, 2021.

Jia, A., Liang, S., Wang, D., Ma, L., Wang, Z., and Xu, S.: Global hourly, 5 km, all-sky land surface temperature data from 2011 to 2021 based on integrating geostationary and polar-orbiting satellite data, Earth Syst. Sci. Data Discuss., 1–35, https://doi.org/10.5194/essd-2022-284, 2022.

Jiang, G.-M. and Liu, R.: Retrieval of Sea and Land Surface Temperature From SVISSR/FY-2C/D/E Measurements, IEEE 550   Trans. Geosci. Remote Sens., 52, 6132–6140, https://doi.org/10.1109/TGRS.2013.2295260, 2014.

Jin, M. and Dickinson, R. E.: A generalized algorithm for retrieving cloudy sky skin temperature from satellite thermal infrared radiances, J. Geophys. Res. Atmospheres, 105, 27037–27047, https://doi.org/10.1029/2000JD900318, 2000.

Kruse, F., Lefkoff, A., Boardman, J., Heidebrecht, K., Shapiro, A., Barloon, P., and Goetz, A.: The Spectral Image-Processing System (sips) - Interactive Visualization and Analysis of Imaging Spectrometer Data, Remote Sens. Environ., 44, 145–163, 555   https://doi.org/10.1016/0034-4257(93)90013-N, 1993.

Li, B., Liang, S., Liu, X., Ma, H., Chen, Y., Liang, T., and He, T.: Estimation of all-sky 1 km land surface temperature over the conterminous United States, Remote Sens. Environ., 266, 112707, https://doi.org/10.1016/j.rse.2021.112707, 2021a.

Li, H., Chai, L., Crow, W., Dong, J., Liu, S., and Zhao, S.: The reliability of categorical triple collocation for evaluating soil freeze/ thaw datasets, REMOTE Sens. Environ., 281, https://doi.org/10.1016/j.rse.2022.113240, 2022.

560   Li, K., Chen, Y., and Gao, S.: Comparative Analysis of Variations and Patterns between Surface Urban Heat Island Intensity and Frequency across 305 Chinese Cities, Remote Sens., 13, 3505, https://doi.org/10.3390/rs13173505, 2021b.

Li, W., Weng, B., Yan, D., Lai, Y., Li, M., and Wang, H.: Underestimated permafrost degradation: Improving the TTOP model based on soil thermal conductivity, Sci. TOTAL Environ., 854, https://doi.org/10.1016/j.scitotenv.2022.158564, 2023a.

Li, X., Cheng, G., Liu, S., Xiao, Q., Ma, M., Jin, R., Che, T., Liu, Q., Wang, W., Qi, Y., Wen, J., Li, H., Zhu, G., Guo, J., Ran, 565   Y., Wang, S., Zhu, Z., Zhou, J., Hu, X., and Xu, Z.: Heihe Watershed Allied Telemetry Experimental Research (HiWATER): Scientific Objectives and Experimental Design, Bull. Am. Meteorol. Soc., 94, 1145–1160, https://doi.org/10.1175/BAMS-D-12-00154.1, 2013a.

Li, X., Zhou, Y., Asrar, G. R., and Zhu, Z.: Creating a seamless 1km resolution daily land surface temperature dataset for urban and surrounding areas in the conterminous United States, Remote Sens. Environ., 206, 84–97, 570   https://doi.org/10.1016/j.rse.2017.12.010, 2018.

Li, Z.-L., Tang, B.-H., Wu, H., Ren, H., Yan, G., Wan, Z., Trigo, I. F., and Sobrino, J. A.: Satellite-derived land surface temperature: Current status and perspectives, Remote Sens. Environ., 131, 14–37, https://doi.org/10.1016/j.rse.2012.12.008, 2013b.

Li, Z.-L., Wu, H., Duan, S.-B., Zhao, W., Ren, H., Liu, X., Leng, P., Tang, R., Ye, X., Zhu, J., Sun, Y., Si, M., Liu, M., Li, J.,
575   Zhang, X., Shang, G., Tang, B.-H., Yan, G., and Zhou, C.: Satellite Remote Sensing of Global Land Surface Temperature:
Definition, Methods, Products, and Applications, Rev. Geophys., 61, e2022RG000777,
https://doi.org/10.1029/2022RG000777, 2023b.

Liao, Y., Shen, X., Zhou, J., Ma, J., Zhang, X., Tang, W., Chen, Y., Ding, L., and Wang, Z.: Surface urban heat island detected
by all-weather satellite land surface temperature, Sci. Total Environ., 811, 151405,
580   https://doi.org/10.1016/j.scitotenv.2021.151405, 2022.

Liu, H., Dong, W., Fu, C., and Beijing: The Long-Term Field Experiment on Aridification and the Ordered HumanActivity in
Semi-Arid Area at Tongyu, Northeast China, Clim. Environ. Res., 2004.

Liu, S., Li, X., Xu, Z., Che, T., Xiao, Q., Ma, M., Liu, Q., Jin, R., Guo, J., Wang, L., Wang, W., Qi, Y., Li, H., Xu, T., Ran,
Y., Hu, X., Shi, S., Zhu, Z., Tan, J., Zhang, Y., and Ren, Z.: The Heihe Integrated Observatory Network: A Basin-Scale Land
585   Surface Processes Observatory in China, Vadose Zone J., 17, 180072, https://doi.org/10.2136/vzj2018.04.0072, 2018.

Liu, S. M., Xu, Z. W., Wang, W. Z., Jia, Z. Z., Zhu, M. J., Bai, J., and Wang, J. M.: A comparison of eddy-covariance and
large aperture scintillometer measurements with respect to the energy balance closure problem, Hydrol. Earth Syst. Sci., 15,
1291–1306, https://doi.org/10.5194/hess-15-1291-2011, 2011.

Liu, S. M., Xu, Z. W., Zhu, Z. L., Jia, Z. Z., and Zhu, M. J.: Measurements of evapotranspiration from eddy-covariance systems
590   and large aperture scintillometers in the Hai River Basin, China, J. Hydrol., 487, 24–38,
https://doi.org/10.1016/j.jhydrol.2013.02.025, 2013.

Liu, Y., Hiyama, T., and Yamaguchi, Y.: Scaling of land surface temperature using satellite data: A case examination on
ASTER and MODIS products over a heterogeneous terrain area, Remote Sens. Environ., 105, 115–128,
https://doi.org/10.1016/j.rse.2006.06.012, 2006.

595   Long, D., Yan, L., Bai, L., Zhang, C., Li, X., Lei, H., Yang, H., Tian, F., Zeng, C., Meng, X., and Shi, C.: Generation of
MODIS-like land surface temperatures under all-weather conditions based on a data fusion approach, Remote Sens. Environ.,
246, 111863, https://doi.org/10.1016/j.rse.2020.111863, 2020.

Ma, J., Zhou, J., Liu, S., Göttsche, F.-M., Zhang, X., Wang, S., and Li, M.: Continuous evaluation of the spatial
representativeness of land surface temperature validation sites, Remote Sens. Environ., 265, 112669,
600   https://doi.org/10.1016/j.rse.2021.112669, 2021.

Ma, Y., Yao, T., and Wang, J.: Experimental study of energy and water cycle in Tibetan Plateau: The progress introduction on
the study of GAME/Tibet and CAMP/Tibet, Plateau Meteorol., 25, 344–351, 2006.

Ma, Y., Zhou, J., Liu, S., Zhang, W., Zhang, Y., Xu, Z., Song, L., and Zhao, H.: Estimation of evapotranspiration using all-
weather land surface temperature and variational trends with warming temperatures for the River Source Region in Southwest
605   China, J. Hydrol., 613, 128346, https://doi.org/10.1016/j.jhydrol.2022.128346, 2022.

Martins, J. P. A., Trigo, I. F., Ghilain, N., Jimenez, C., Göttsche, F.-M., Ermida, S. L., Olesen, F.-S., Gellens-Meulenberghs,
F., and Arboleda, A.: An All-Weather Land Surface Temperature Product Based on MSG/SEVIRI Observations, Remote Sens.,
11, 3044, https://doi.org/10.3390/rs11243044, 2019.

Metz, M., Andreo, V., and Neteler, M.: A New Fully Gap-Free Time Series of Land Surface Temperature from MODIS LST
610   Data, Remote Sens., 9, 1333, https://doi.org/10.3390/rs9121333, 2017.

Mildrexler, D. J., Zhao, M., Cohen, W. B., Running, S. W., Song, X. P., and Jones, M. O.: Thermal Anomalies Detect Critical Global Land Surface Changes, J. Appl. Meteorol. Climatol., 57, 391–411, 2018.

Muñoz-Sabater, J., Dutra, E., Agustí-Panareda, A., Albergel, C., Arduini, G., Balsamo, G., Boussetta, S., Choulga, M., Harrigan, S., Hersbach, H., Martens, B., Miralles, D. G., Piles, M., Rodríguez-Fernández, N. J., Zsoter, E., Buontempo, C., and Thépaut, J.-N.: ERA5-Land: a state-of-the-art global reanalysis dataset for land applications, Earth Syst. Sci. Data, 13, 4349–4383, https://doi.org/10.5194/essd-13-4349-2021, 2021.

Parinussa, R., Lakshmi, V., Johnson, F., and Sharma, A.: Comparing and Combining Remotely Sensed Land Surface Temperature Products for Improved Hydrological Applications, Remote Sens., 8, 162, https://doi.org/10.3390/rs8020162, 2016.

Pastorello, G., Trotta, C., Canfora, E., Chu, H., Christianson, D., Cheah, Y.-W., Poindexter, C., Chen, J., Elbashandy, A., Humphrey, M., Isaac, P., Polidori, D., Reichstein, M., Ribeca, A., van Ingen, C., Vuichard, N., Zhang, L., Amiro, B., Ammann, C., Arain, M. A., Ardö, J., Arkebauer, T., Arndt, S. K., Arriga, N., Aubinet, M., Aurela, M., Baldocchi, D., Barr, A., Beamesderfer, E., Marchesini, L. B., Bergeron, O., Beringer, J., Bernhofer, C., Berveiller, D., Billesbach, D., Black, T. A., Blanken, P. D., Bohrer, G., Boike, J., Bolstad, P. V., Bonal, D., Bonnefond, J.-M., Bowling, D. R., Bracho, R., Brodeur, J., Brümmer, C., Buchmann, N., Burban, B., Burns, S. P., Buysse, P., Cale, P., Cavagna, M., Cellier, P., Chen, S., Chini, I., Christensen, T. R., Cleverly, J., Collalti, A., Consalvo, C., Cook, B. D., Cook, D., Coursolle, C., Cremonese, E., Curtis, P. S., D'Andrea, E., da Rocha, H., Dai, X., Davis, K. J., Cinti, B. D., Grandcourt, A. de, Ligne, A. D., De Oliveira, R. C., Delpierre, N., Desai, A. R., Di Bella, C. M., Tommasi, P. di, Dolman, H., Domingo, F., Dong, G., Dore, S., Duce, P., Dufrêne, E., Dunn, A., Dušek, J., Eamus, D., Eichelmann, U., ElKhidir, H. A. M., Eugster, W., Ewenz, C. M., Ewers, B., Famulari, D., Fares, S., Feigenwinter, I., Feitz, A., Fensholt, R., Filippa, G., Fischer, M., Frank, J., Galvagno, M., et al.: The FLUXNET2015 dataset and the ONEFlux processing pipeline for eddy covariance data, Sci. Data, 7, 225, https://doi.org/10.1038/s41597-020-0534-3, 2020.

Peng, S.-S., Piao, S., Zeng, Z., Ciais, P., Zhou, L., Li, L. Z. X., Myneni, R. B., Yin, Y., and Zeng, H.: Afforestation in China cools local land surface temperature, Proc. Natl. Acad. Sci. U. S. A., 111, 2915–2919, https://doi.org/10.1073/pnas.1315126111, 2014.

Qu, Y., Zhu, Z., Montzka, C., Chai, L., Liu, S., Ge, Y., Liu, J., Lu, Z., He, X., Zheng, J., and Han, T.: Inter-comparison of several soil moisture downscaling methods over the Qinghai-Tibet Plateau, China, J. Hydrol., 592, 125616, https://doi.org/10.1016/j.jhydrol.2020.125616, 2021.

Rodell, M., Houser, P. R., Jambor, U., Gottschalck, J., Mitchell, K., Meng, C.-J., Arsenault, K., Cosgrove, B., Radakovich, J., Bosilovich, M., Entin, J. K., Walker, J. P., Lohmann, D., and Toll, D.: The Global Land Data Assimilation System, Bull. Am. Meteorol. Soc., 85, 381–394, https://doi.org/10.1175/BAMS-85-3-381, 2004.

Sandeep, P., Reddy, G. P. O., Jegankumar, R., and Kumar, K. C. A.: Monitoring of agricultural drought in semi-arid ecosystem of Peninsular India through indices derived from time-series CHIRPS and MODIS datasets, Ecol. Indic., 121, 107033, https://doi.org/10.1016/j.ecolind.2020.107033, 2021.

Sims, D. A., Rahman, A. F., Cordova, V. D., El-Masri, B. Z., Baldocchi, D. D., Bolstad, P. V., Flanagan, L. B., Goldstein, A. H., Hollinger, D. Y., Misson, L., Monson, R. K., Oechel, W. C., Schmid, H. P., Wofsy, S. C., and Xu, L.: A new model of gross primary productivity for North American ecosystems based solely on the enhanced vegetation index and land surface temperature from MODIS, Remote Sens. Environ., 112, 1633–1646, https://doi.org/10.1016/j.rse.2007.08.004, 2008.

Wan, Z.: New refinements and validation of the collection-6 MODIS land-surface temperature/emissivity product, Remote Sens. Environ., 140, 36–45, https://doi.org/10.1016/j.rse.2013.08.027, 2014.

Wang, B., Gao, P., Niu, X., and Sun, J.: Policy-driven China's Grain to Green Program: Implications for ecosystem services, Ecosyst. Serv., 27, 38–47, https://doi.org/10.1016/j.ecoser.2017.07.014, 2017.

Wen J., Lan Y., Su Z., Tian H., Shi X., Zhang Y., Wang X., Liu R., Zhang T., Kang Y., Lv S., and Zhang J.: Advances in observation and modeling of land surface processes over the source region of the Yellow River, Adv. Earth Sci., 26, 575–585, 2011.

Weng, Q. and Fu, P.: Modeling annual parameters of clear-sky land surface temperature variations and evaluating the impact of cloud cover using time series of Landsat TIR data, Remote Sens. Environ., 140, 267–278, https://doi.org/10.1016/j.rse.2013.09.002, 2014.

Wu, P., Shen, H., Zhang, L., and Göttsche, F.-M.: Integrated fusion of multi-scale polar-orbiting and geostationary satellite observations for the mapping of high spatial and temporal resolution land surface temperature, Remote Sens. Environ., 156, 169–181, https://doi.org/10.1016/j.rse.2014.09.013, 2015.

Xu, S., Cheng, J., and Zhang, Q.: A Random Forest-Based Data Fusion Method for Obtaining All-Weather Land Surface Temperature with High Spatial Resolution, Remote Sens., 13, 2211, https://doi.org/10.3390/rs13112211, 2021.

Xu, Z., Liu, S., Li, X., Shi, S., Wang, J., Zhu, Z., Xu, T., Wang, W., and Ma, M.: Intercomparison of surface energy flux measurement systems used during the HiWATER-MUSOEXE, J. Geophys. Res. Atmospheres, 118, 13,140-13,157, https://doi.org/10.1002/2013JD020260, 2013.

Yang, J. and Huang, X.: The 30 m annual land cover dataset and its dynamics in China from 1990 to 2019, Earth Syst. Sci. Data, 13, 3907–3925, https://doi.org/10.5194/essd-13-3907-2021, 2021.

Yang, J., Zhou, J., Göttsche, F.-M., Long, Z., Ma, J., and Luo, R.: Investigation and validation of algorithms for estimating land surface temperature from Sentinel-3 SLSTR data, Int. J. Appl. Earth Obs. Geoinformation, 91, 102136, https://doi.org/10.1016/j.jag.2020.102136, 2020.

Yao, R., Wang, L., Huang, X., Cao, Q., Wei, J., He, P., Wang, S., and Wang, L.: Global seamless and high-resolution temperature dataset (GSHTD), 2001–2020, Remote Sens. Environ., 286, 113422, https://doi.org/10.1016/j.rse.2022.113422, 2023.

Yu, P., Zhao, T., Shi, J., Ran, Y., Jia, L., Ji, D., and Xue, H.: Global spatiotemporally continuous MODIS land surface temperature dataset, Sci. Data, 9, 143, https://doi.org/10.1038/s41597-022-01214-8, 2022.

Zhai, J., Wang, L., Liu, Y., Wang, C., and Mao, X.: Assessing the effects of China's Three-North Shelter Forest Program over 40 years, Sci. Total Environ., 857, 159354, https://doi.org/10.1016/j.scitotenv.2022.159354, 2023.

Zhan, W., Chen, Y., Zhou, J., Wang, J., Liu, W., Voogt, J., Zhu, X., Quan, J., and Li, J.: Disaggregation of remotely sensed land surface temperature: Literature survey, taxonomy, issues, and caveats, Remote Sens. Environ., 131, 119–139, https://doi.org/10.1016/j.rse.2012.12.014, 2013.

Zhang, J. and Han, S.: FLUXNET2015 CN-Cha Changbaishan, FluxNet; IAE Chinese Academy of Sciences, https://doi.org/10.18140/FLX/1440137, 2016.

Zhang, L., Jiao, W., Zhang, H., Huang, C., and Tong, Q.: Studying drought phenomena in the Continental United States in 2011 and 2012 using various drought indices, Remote Sens. Environ., 190, 96–106, https://doi.org/10.1016/j.rse.2016.12.010, 2017.

Zhang, T., Zhou, Y., Zhu, Z., Li, X., and Asrar, G. R.: A global seamless 1 km resolution daily land surface temperature dataset (2003–2020), Earth Syst. Sci. Data, 14, 651–664, https://doi.org/10.5194/essd-14-651-2022, 2022.

690 Zhang, X., Zhou, J., Göttsche, F.-M., Zhan, W., Liu, S., and Cao, R.: A Method Based on Temporal Component Decomposition for Estimating 1-km All-Weather Land Surface Temperature by Merging Satellite Thermal Infrared and Passive Microwave Observations, IEEE Trans. Geosci. Remote Sens., 57, 4670–4691, https://doi.org/10.1109/TGRS.2019.2892417, 2019.

Zhang, X., Zhou, J., Liang, S., Chai, L., Wang, D., and Liu, J.: Estimation of 1-km all-weather remotely sensed land surface temperature based on reconstructed spatial-seamless satellite passive microwave brightness temperature and thermal infrared data, ISPRS J. Photogramm. Remote Sens., 167, 321–344, https://doi.org/10.1016/j.isprsjprs.2020.07.014, 2020.

695 Zhang, X., Zhou, J., Liang, S., and Wang, D.: A practical reanalysis data and thermal infrared remote sensing data merging (RTM) method for reconstruction of a 1-km all-weather land surface temperature, Remote Sens. Environ., 260, 112437, https://doi.org/10.1016/j.rse.2021.112437, 2021.

Zhang, Y.-R., Shang, G.-F., Leng, P., Ma, C., Ma, J., Zhang, X., and Li, Z.-L.: Estimation of quasi-full spatial coverage soil moisture with fine resolution in China from the combined use of ERA5-Land reanalysis and TRIMS land surface temperature 700 product, Agric. WATER Manag., 275, https://doi.org/10.1016/j.agwat.2022.107990, 2023.

Zhao, W. and Duan, S.-B.: Reconstruction of daytime land surface temperatures under cloud-covered conditions using integrated MODIS/Terra land products and MSG geostationary satellite data, Remote Sens. Environ., 247, 111931, https://doi.org/10.1016/j.rse.2020.111931, 2020.

Zhou, J., Zhang, X., Tang, W., Ding, L., Ma, J., Zhang, X. Daily 1-km all-weather land surface temperature dataset for the

705 Chinese landmass and its surrounding areas (TRIMS LST; 2000-2021). National Tibetan Plateau/Third Pole Environment Data

Center [data set], https://doi.org/10.11888/Meteoro.tpdc.271252, 2021.

Zhou, J., Zhang, X., Zhan, W., Göttsche, F.-M., Liu, S., Olesen, F.-S., Hu, W., and Dai, F.: A Thermal Sampling Depth Correction Method for Land Surface Temperature Estimation From Satellite Passive Microwave Observation Over Barren 710 Land, IEEE Trans. Geosci. Remote Sens., 55, 4743–4756, https://doi.org/10.1109/TGRS.2017.2698828, 2017.

Zhu, X., Duan, S.-B., Li, Z.-L., Wu, P., Wu, H., Zhao, W., and Qian, Y.: Reconstruction of land surface temperature under cloudy conditions from Landsat 8 data using annual temperature cycle model, Remote Sens. Environ., 281, 113261, https://doi.org/10.1016/j.rse.2022.113261, 2022.